Title

Synthesis, Structure, & Thermodynamics of High Uranium Content Iron Oxides

Author

Lam, Andy

Publication Date

2021

Synthesis, Structure, & Thermodynamics of High Uranium Content Iron Oxides

By

ANDY LAM

DISSERTATION

Submitted in partial satisfaction of the requirements for the degree of

DOCTOR OF PHILOSOPHY

in

Materials Science and Engineering

in the

OFFICE OF GRADUATE STUDIES

of the

UNIVERSITY OF CALIFORNIA

DAVIS

Approved:

Alexandra Navrotsky, Chair

Jesús M. Velázquez

William Casey

Committee in Charge

2021

Abstract

Iron oxides may reside in an abundance of environments where their chemical and physical properties may assist in combating repercussions of human industrialization. Uranium species, such as from leaked radiological waste repositories or from ore mine tailings, may easily mobilize and spread throughout their immediate aqueous environments. Readily present iron oxide nanoparticles may favorably adsorb these radiotoxic contaminants and limit the extent by which the actinide may spread by. They may further inhibit their mobility by trapping the atoms within their structures – a mechanism which we utilize and offer as a potential filtration and processing method. This dissertation aims to address the lack of thermodynamic data for uranium-incorporated iron oxide polymorphs. Results from this work may assist in understanding the fate of uranium in geological disposal sites over extended timescales and the transport of uranium in the environment. These insights will help guide the improvement of safe and scalable radioactive waste practices and water remediation applications, which ultimately improve water safety for humans and surrounding ecosystems.

Chapter 2 discusses the role that uranium incorporation plays on the structure and thermodynamic stability of hematite. The synthesis method for these samples addresses challenges present in existing literature, namely high uranium concentrations and largely reduced reaction times. Formation enthalpies relative to constituent U and Fe oxides become increasingly positive with increasing uranium content. Based on structural measurements and calculations, the described coprecipitation and accelerated hydrothermal treatment process produce $U_xFe_{2-2x}O_3$ analogous to conventionally aged samples studied in previous literature.

Chapter 3 expands this work to explore U-Fe interactions in conditions where goethite, rather than hematite, is the energetically favorable polymorph. This chapter provides an alternative

synthesis method for uranium incorporation into goethite, using strictly Fe(III) solutions as opposed to conventional mixtures of Fe(II) and Fe(III). Thermodynamic and structural studies were then employed to discern the stability of uranium incorporation, as well as the mechanism by which this occurs under previously unexplored aerobic synthesis conditions.

Chapter 4 provides supplemental work by exploring kinetics and thermodynamics of aging synthetic ferrihydrite colloids. These metastable, poorly ordered nanoparticles gradually crystallize and transform into hematite. Measured calorimetric data were analyzed with existing data on ferrihydrites and nanosized goethite. Results highlight the time frame in which the formation enthalpy of 2-line ferrihydrite sharply drops, possibly indicative of the amorphous colloids beginning to crystallize and stabilize. Continued work may validate this hypothesis and elucidate the local atomistic behavior during this structural transition.

Chapter 5 concludes with currenting findings, as well as future directions that this work may be taken to.

Appendix A provides supporting information for uranium-incorporated hematite experiments.

Appendix B provides supporting information for uranium-incorporated goethite experiments.

Acknowledgements

I thank my advisors Prof. Alexandra Navrotsky and Prof. Jesús Velázquez for their compassion and for guiding me as a researcher. Thank you for accepting me, for continuously supporting me, and ultimately for caring about my wellbeing and success. Thank you for cultivating environments in which I have so many fond memories.

I would like to thank the members of my qualifying exam committee: Prof. Bill Casey, Prof. Ricardo Castro, Prof. Shirley Chiang, Prof. Roopali Kukreja, and Prof. Yayoi Takamura. I also thank Prof. Bill Casey for his support as part of my dissertation committee, alongside my advisors Prof. Navrotsky and Prof. Velázquez.

Members of the former Peter A. Rock Thermochemistry Laboratory and of the Center for Materials of the Universe (MotU) at Arizona State University, thank you. Members of the Velázquez research group, thank you. Thank you to all the postdocs, grad students, visiting researchers, instructors, and administrators whom I have had the pleasure of interacting with these past five years.

I am particularly grateful to Novendra Novendra and Pinghui Zhang for our virtual writing sessions to get through our dissertations amid the COVID-19 pandemic. Dr. Lili Wu, Novendra Novendra, and Casey Sugie, thank you for making the office an inviting and fun place to be. Dr. Anna Shelyug, thank you for being a positive role model, and thank you for showing me the ropes in the radioactive materials lab and the calorimetry suite.

William Cook, Suki LaForga, Marlene Slichter.

Dr. Bin Wang, Dr. Can Agca, Dr. Jiewei Chen, Dr. Zamir Akimbekov.

Dr. Kat Armstrong, Dr. Tamilarasan Subramani, Dr. Xin Guo, Dr. Geetu Sharma, Dr. Anastasia Koryttseva.

Dr. Sergey Ushakov, Krasen Kovachev, George Wayrynen. Dr. Pardha Saradhi Maram, Dr. Kristina Lilova.

Jessica Ortiz, Brian Wuille Bille, Fatima Hussain, Joseph Perryman, Kabian Ritter, Forrest Hyler, Rowan Brower, Joshua Jude, Julio Zamora, Maria Chang, Dr. Ivonne Ferrer.

Grace Woods and Prof. Jeff Gibeling, thank you for helping me navigate through PhD process and ensuring that I reach the finish line. I also acknowledge and thank the following sources of funding that enabled me to carry out my research:

- Towards Outstanding Postgraduate Students (TOPS) Award; UCD CoE and Depts of CHE and MSE
- Enrique Lavernia Graduate Fellowship; donors in honor of work by former Dean Enrique Lavernia
- Grant DE-FG02-97ER14749 (Thermodynamics of Minerals Stable near Earth's Surface); U.S. Department of Energy, Office of Basic Energy Sciences
- Advancing Scientific Careers to Enhance Nuclear Technologies (ASCENT) grant; Nuclear Regulatory Commission (NRC)

I extend my gratitude to Prof. Sam Shaw and Prof. Katherine Morris for inviting me to work with them at the University of Manchester. Thank you to Olwen Stagg, Dr. Luke Townsend, and Dr. Thomas Neill. And I thank the many other members of The Research Centre for Radwaste and Decommissioning for their incredible kindness and thoughtful discussions throughout my stay.

Prof. Daniel Mumm (UCI) and Prof. Martha Mecartney (UCI), thank you for accepting me into your labs during my undergraduate studies. Prof. Farghalli Mohamed (UCI), thank you for inspiring me to immerse myself in the world of materials science. To my mentors Dr. Matt Weeks (WD, UCI), Dr. Kara Philips (UCI), and Dr. Todd Matsubara (UCI), thank you for planting in me the thought of pursuing a PhD.

I am immensely grateful for the friends I lived with for nearly the entirety of my program here at Davis: Bradley Harris, Michael Bull, and Kristen Le. Their unwavering friendship and support kept me afloat when I was struggling the most. I also thank Brian Hoang, Adele Halili, and Allison Huang for their many years of friendship.

I thank my parents and my sisters for supporting me in every way they could and for helping shape who I am today. I also dedicate this work to my grandparents whom I lost during this time.

I struggle to fully express my gratitude to every person who has helped me on this journey.

I appreciate the many people I have met throughout this process.

Thank you.

Table of Contents

Chapter 1

Introduction

1.1 Uranium-Iron Oxide Interactions

1.1.1 Nuclear Waste and the Environment

Radioactive waste, such as spent uranium oxide fuel or processed waste sludge, must be safely stored in isolation for thousands of years. Nuclear waste from energy and weapons research in the 20th century persist in a wide variety of chemical and physical compositions, each of which pose their own challenges for treatment and storage. The treatment and extraction processes used at nuclear research facilities in the United States throughout the years have varied. As a result, waste storage tanks may contain a variety of constituents that may continue to interact with the contained radionuclides.[1–5] These processes were used to extract and reprocess useful transuranic elements from the waste. Unextracted portions would remain in the tank and are by no means harmless. Such tanks may also leak and dispense their contents to their immediate environments. Sludge waste stored at the U.S. DOE Hanford Site, in addition to uranyl(VI) complexes and precipitates, has been found to contain various iron-bearing phases, including hematite, goethite, ferrihydrite, and maghemite.[5,6] Aqueous components of radioactive waste streams include dissolved metals, nitrates, sulfates, and phosphates.[6–12] The amalgamation of constituents and variability in extreme conditions between storage tanks create complex consequences to radionuclide kinetics and thermodynamics. This represents just one category of waste streams where uranium and other radionuclides pose environmental and public health threats. These forms of waste may be processed in preparation for long term storage in geological repositories, which then pose new challenges and contamination risks.

The method of vitrifying transuranic waste and storing it underground may result in its eventual exposure and leaching into groundwater. The cementitious backfill material to be used in these settings may dissolve and produce highly basic conditions localized around the waste, which would drive forward corrosion of the vitrified waste.[13,14] Additionally, higher concentrations of stored radioactive waste may increase the local temperature to 50 – 100 °C.[15] This elevated temperature will accelerate corrosion processes and may dictate the favored crystallization of different iron oxide phases coming from the corrosion of steel.[16]

1.1.2 Uranium Immobilization by Iron Oxides

Research performed by Duff et al. experimentally demonstrated the ability for uranium to exist within the hematite crystal structure with the same coordination environment as that of the iron atom, in the form of coprecipitated uranium trioxide (γ-UO_3).[17,18] The more distorted octahedra of uranium-coordinated hematite relative to conventional coordination may have been partially attributed to the larger ionic radius of U(VI) (0.72 – 0.80 Å) relative to Fe(III) (0.65 Å), as well as the possible charge compensation mechanism of an additional Fe(III) vacancy.[19] This distortion may be reason for a limited saturation limit of uranium within the lattice, although that point has not yet been identified.

Following the work by Duff et al., numerous studies have been performed to study adsorptive properties of nanoscale Fe(III) oxides, where the increased surface area facilitates increased uranium loadings.[20,21] Continued crystallization of various iron oxides in the presence of uranium was shown to result in greater resistance against uranium loss and remobilization in carbonate solutions.[22] Hydrous ferric oxides that have been allowed to crystallize with uranium for longer periods of time resulted in less uranium extracted back out, with the difference growing more pronounced at longer extraction times. As the iron oxide particles grow, adsorbed uranium is not released back into the solution. This may be attributed to some uranium being trapped within the lattice as Ostwald ripening of the mineral occurs. Encasing the uranium within the structure protects it from direct contact with the solution that would otherwise remobilize it.

Subsequent experimental studies with nanocrystalline iron oxides have demonstrated that they structurally incorporate U(VI) within mineral lattices, specifically within cation sites of iron oxides.[23,24] Marshall et al. proposed a distinct difference in incorporated uranium compared to the mechanism proposed by Duff et al.[23] Rather than forming a distinct uranium trioxide phase, Marshall et al. concluded that the uranium could instead occupy iron sites and bond with oxygen atoms in the distorted hematite octahedra. The different proposed uranium immobilization mechanisms may involve different degrees of energetics, resulting in different overall stabilities of the uranium-loaded iron oxide. While there does not yet appear to be wide consensus on the exact incorporation and charge balance mechanism of uranium into hematite or other Fe(III) oxides, it is possible to determine how thermodynamically stable these uranium-incorporated iron oxides are.

Because iron oxides can be fine-grained and have large surface areas, uranium will also adsorb on these surfaces.[3,25–27] The high adsorptive performance of iron oxides is made more attractive by their natural abundance and environmental benignity. Another consequence of higher surface area is a more pronounced effect of surface energy on formation enthalpy. Different iron oxide polymorphs have different surface energies, resulting in linear size dependencies of formation enthalpies that may cross over each other. As a result, it is possible for a phase that is metastable relative to another phase at the bulk scale to become the more favorable polymorph when comparing at higher specific surface areas. For example, goethite becomes energetically favorable relative to hematite at the nanoscale.[28] Significant amounts of uranium incorporation within different iron oxide lattice structures may affect surface energetics as well as bulk formation enthalpies.

The readily present iron oxides, both from the local environment and from corroded steel enclosures, may play a significant role in inhibiting the mobility of escaped uranium. The competition between surface sorption and lattice incorporation is an important factor in determining uranium retention. Understanding the energetic driving forces behind lattice incorporation and surface sorption is imperative. Determination of its energetics will assist in understanding the role of these materials in retarding U(VI) mobility over the course of millennia.

1.2 Dissertation Objectives

Now that studies have confirmed the ability of hematite to incorporate uranium atoms within its structure, questions that come to mind are how much incorporation can occur, and how stable this immobilized material is. Synthesis of hematite nanoparticles is thoroughly detailed in literature, including in the presence of uranium. However, there is still a lack of thermodynamic data to supplement current knowledge on this system. Without such data, it remains unknown whether uranium may favorably escape from the structure and remobilize over time. Upon completion of thermodynamic measurements and calculations for hematite with varying amounts of uranium incorporation, the research project will expand with the synthesis of other uranium-loaded Fe(III) oxides.

Results from this project will provide data essential for understanding the fate of uranium in geological disposal sites over extended timescales and the transport of uranium in the environment. Identifying the stability of structural incorporation, or lack thereof, will indicate the feasibility of iron oxides inhibiting the mobility of leached uranium. These insights will help guide the improvement of safe and scalable radioactive waste practices and water remediation applications, which ultimately improve water safety for humans and surrounding ecosystems.

1.2.1 Hydrothermal Synthesis of U-Fe Oxides

Early experimental studies of uranium adsorption onto iron oxides were done by aging a mixture of hematite and goethite at 25°C for up to 3 years.[29] In 2002, Duff et. al. accelerated to the aging process down to one month by coprecipitating the uranium-iron oxide at 60°C but retains the inability to consistently produce a single iron oxide phase.[18] Different iron oxides may have different adsorption affinities and cation incorporation mechanisms. The abundance of dimensions convolute uranium incorporation data where more than a single phase is present. This synthesis route has continued to be followed in recent years.

Here, we instead hydrothermally synthesize uranium-incorporated hematite. Chemicals and conditions for synthesis are adapted from published works on hydrothermal synthesis of bare iron oxide nanoparticles and on coprecipitation of uranium polymorphs such as hematite and goethite.[23,30] One primary advantage over conventional coprecipitation methods is the ability to establish conditions conducive towards only a single polymorph is thermodynamically driven to crystallize. The second advantage and motivation behind this method is reduced reaction times. Syntheses commonly range from 24 to 72 hours rather than the weeks, months, or even years of conventional aging. Synthesizing iron oxides without the presence of secondary polymorphs is essential for accurately attributing calorimetric measurements to its respective polymorph. The drastic reduction in synthesis time makes modifying conditions for different uranium loadings and particle sizes more practical. Doing so may better represent possible amounts of uranium immobilization that may occur under geological waste storage conditions.

1.2.2 Thermodynamic Perspective

High temperature oxide melt solution calorimetry will be employed to characterize the thermodynamic properties of synthesized uranium-bearing iron oxides. A custom-built Tian-Calvet calorimeter is used to measure the dissolution enthalpy of each sample within molten oxide solvents at 700-800 °C.[31–33] This form of calorimetry is capable of dissolving highly stable minerals, and an extensive collection of iron-bearing and uranium-bearing minerals have previously been measured using this technique.[34–39] Thermochemical cycles combine measured and published calorimetric data to calculate formation enthalpies of the mixed U-Fe oxides at ambient temperature. These formation enthalpies are obtained for varying amounts of uranium incorporation, such that the enthalpies may be plotted as a function of uranium to observe a trend in stability.

It is hypothesized that the formation enthalpy of iron oxides will change as a function of uranium concentration within the lattice. Formation enthalpies of the uranium-incorporated iron oxides will be compared to calculated formation enthalpies of proportional amounts of constituent elements or binary oxides. This comparison will determine whether incorporation results in stabilities representative of proportional sums of their respective oxides, or whether special interactions are significantly altering its stability.

1.3 References

1. Ryan, J. N. & Elimelech, M. Colloid mobilization and transport in groundwater. *Colloids Surfaces A Physicochem. Eng. Asp.* **107**, 1–56 (1996).

2. Gephart, R. E. A Short History of Hanford Waste Generation, Storage, and Release. *PNNL-13605* 1–39 (2003).

3. Dong, W., Tokunaga, T. K., Davis, J. A. & Wan, J. Uranium(VI) adsorption and surface complexation modeling onto background sediments from the F-Area Savannah River site. *Environ. Sci. Technol.* **46**, 1565–1571 (2012).

4. Chen, A., Shang, C., Shao, J., Zhang, J. & Huang, H. The application of iron-based technologies in uranium remediation: A review. *Sci. Total Environ.* **575**, 1291–1306 (2017).

5. Peterson, R. A. *et al.* Review of the Scientific Understanding of Radioactive Waste at the U.S. DOE Hanford Site. *Environ. Sci. Technol.* **52**, 381–396 (2018).

6. Geeting, J. G. H. & Hallen, R. T. Filtration, Washing, and Caustic Leaching of Hanford Tank AZ-101 Sludge. *Sep. Sci. Technol.* **40**, 1–15 (2005).

7. Coleman, C. *Compositing and Characterization of Samples from Hanford Tank 241-AY-102/ C-106*. (2004). doi:10.2172/821389

8. Edwards, M. K. *et al. Characterization, Leaching, and Filtration Testing for Tributyl Phosphate (TBP, Group 7) Actual Waste Sample Composites*. (2009). doi:10.2172/961676

9. Shimskey, R. W. *et al. Filtration and Leach Testing for REDOX Sludge and S-Saltcake Actual Waste Sample Composites*. (2009). doi:10.2172/953798

10. Krupka, K. M. *et al.* Residual Waste from Hanford Tanks 241-C-203 and 241-C-204. 1. Solids Characterization. *Environ. Sci. Technol.* **40**, 3749–3754 (2006).

11. Felmy, A. R., Xia, Y. & Wang, Z. The solubility product of $NaUO_2PO_4·xH_2O$ determined in phosphate and carbonate solutions. *Radiochim. Acta* **93**, (2005).

12. Ofili, N. E. R., Thetford, A. & Kaltsoyannis, N. Adsorption of U(VI) on Stoichiometric and Oxidised Mackinawite: A DFT Study. *Environ. Sci. Technol.* **54**, 6792–6799 (2020).

13. Bots, P. *et al.* Formation of Stable Uranium(VI) Colloidal Nanoparticles in Conditions Relevant to Radioactive Waste Disposal. *Langmuir* **30**, 14396–14405 (2014).

14. Dzaugis, M. E., Spivack, A. J. & D’Hondt, S. A quantitative model of water radiolysis and chemical production rates near radionuclide-containing solids. *Radiat. Phys. Chem.* **115**, 127–134 (2015).

15. Ojovan, M. I., Pankov, A. & Lee, W. E. The ion exchange phase in corrosion of nuclear

waste glasses. *J. Nucl. Mater.* **358**, 57–68 (2006).

16. Dodge, C. J. *et al.* Association of uranium with iron oxides typically formed on corroding steel surfaces. *Environ. Sci. Technol.* **36**, 3504–3511 (2002).
17. Duff, M. C. & Amrhein, C. Uranium(VI) Adsorption on Goethite and Soil in Carbonate Solutions. *Soil Sci. Soc. Am. J.* **60**, 1393–1400 (1996).
18. Duff, M. C., Coughlin, J. U. & Hunter, D. B. Uranium co-precipitation with iron oxide minerals. *Geochim. Cosmochim. Acta* **66**, 3533–3547 (2002).
19. Shannon, R. D. Revised effective ionic radii and systematic studies of interatomic distances in halides and chalcogenides. *Acta Crystallogr. Sect. A* **32**, 751–767 (1976).
20. Zeng, H. *et al.* Nanoscale Size Effects on Uranium(VI) Adsorption to Hematite. *Environ. Sci. Technol.* **43**, 1373–1378 (2009).
21. Ilton, E. S. *et al.* Reduction of U(VI) incorporated in the structure of hematite. *Environ. Sci. Technol.* **46**, 9428–9436 (2012).
22. Smith, S. C., Douglas, M., Moore, D. A., Kukkadapu, R. K. & Arey, B. W. Uranium Extraction From Laboratory-Synthesized, Uranium-Doped Hydrous Ferric Oxides. *Environ. Sci. Technol.* **43**, 2341–2347 (2009).
23. Marshall, T. A. *et al.* Incorporation of Uranium into Hematite during Crystallization from Ferrihydrite. *Environ. Sci. Technol.* **48**, 3724–3731 (2014).
24. McBriarty, M. E. *et al.* Iron Vacancies Accommodate Uranyl Incorporation into Hematite. *Environ. Sci. Technol.* **52**, 6282–6290 (2018).
25. Rossberg, A. *et al.* Identification of uranyl surface complexes on ferrihydrite: Advanced EXAFS data analysis and CD-music modeling. *Environ. Sci. Technol.* **43**, 1400–1406 (2009).
26. Bargar, J. R., Reitmeyer, R., Lenhart, J. J. & Davis, J. A. Characterization of U(VI)-carbonato ternary complexes on hematite: EXAFS and electrophoretic mobility measurements. *Geochim. Cosmochim. Acta* **64**, 2737–2749 (2000).
27. Estes, S. L. & Powell, B. A. Enthalpy of Uranium Adsorption onto Hematite. *Environ. Sci. Technol.* **54**, 15004–15012 (2020).
28. Navrotsky, A., Mazeina, L. & Majzlan, J. Size-driven structural and thermodynamic complexity in iron oxides. *Science* **319**, (2008).
29. Bruno, J., De Pablo, J., Duro, L. & Figuerola, E. Experimental study and modeling of the U(VI)-$Fe(OH)_3$ surface precipitation/coprecipitation equilibria. *Geochim. Cosmochim. Acta* **59**, 4113–4123 (1995).

30. Khalil, M., Yu, J., Liu, N. & Lee, R. L. Hydrothermal synthesis, characterization, and growth mechanism of hematite nanoparticles. *J. Nanoparticle Res.* **16**, 2362 (2014).

31. Navrotsky, A. Progress and new directions in high temperature calorimetry. *Phys. Chem. Miner.* **2**, 89–104 (1977).

32. Navrotsky, A. Progress and new directions in high temperature calorimetry revisited. *Phys. Chem. Miner.* **24**, 222–241 (1997).

33. Navrotsky, A. Progress and New Directions in Calorimetry: A 2014 Perspective. *J. Am. Ceram. Soc.* **97**, 3349–3359 (2014).

34. Majzlan, J., Navrotsky, A. & Evans, B. J. Thermodynamics and crystal chemistry of the hematite-corundum solid solution and the $FeAlO_3$ phase. *Phys. Chem. Miner.* **29**, 515–526 (2002).

35. Majzlan, J., Grevel, K.-D. D. & Navrotsky, A. Thermodynamics of Fe oxides: Part II. Enthalpies of formation and relative stability of goethite (α-FeOOH), lepidocrocite (γ-FeOOH), and maghemite (γ-Fe_2O_3). *Am. Mineral.* **88**, 855–859 (2003).

36. Navrotsky, A., Ma, C., Lilova, K. & Birkner, N. Nanophase Transition Metal Oxides Show Large Thermodynamically Driven Shifts in Oxidation-Reduction Equilibria. *Science.* **330**, 199–201 (2010).

37. Lilova, K. I. *et al.* Oxide melt solution calorimetry of Fe^{2+}-bearing oxides and application to the magnetite-maghemite (Fe_3O_4-$Fe_{8/3}O_4$) system. *Am. Mineral.* **97**, 164–175 (2012).

38. Navrotsky, A., Shvareva, T. & Guo, X. Thermodynamics of uranium minerals and related materials. *Uranium From Cradle to Grave. Mineral. Assoc. Canada Short Courses* **43**, 147–164 (2013).

39. Guo, X. *et al.* Structure and thermodynamics of uranium-containing iron garnets. *Geochim. Cosmochim. Acta* **189**, 269–281 (2016).

Chapter 2

Synthesis and Thermodynamics of Uranium-Incorporated α-Fe_2O_3 Nanoparticles

2.1 Abstract

Hematite nanoparticles were synthesized with U(VI) in circumneutral water through a coprecipitation and hydrothermal treatment process. XRD, TEM, and EXAFS analyses reveal that uranium may aggregate along grain boundaries and occupy Fe sites within hematite. The described synthesis method produces crystalline, single-phase iron oxide nanoparticles absent of surface-bound uranyl complexes. EXAFS data were comparable to spectra from existing studies - whose syntheses were more representative of naturally occurring, extended aging processes. This work provides and validates an accelerated method of synthesizing uranium-immobilized iron oxide nanoparticles for further mechanistic studies. High temperature oxide-melt solution calorimetry measurements were performed to calculate the thermodynamic stability of uranium-incorporated iron oxide nanoparticles. Increasing uranium content within hematite resulted in more positive formation enthalpies. Standard formation enthalpies of $U_xFe_{2-2x}O_3$ were as high as 68.67 ± 3.13 kJ/mol relative to their binary oxides, or -772.26 ± 3.49 kJ/mol relative to their constituent elements, at $x = 0.037$. Data on the thermodynamic stability of uranium retention pathways may assist in predicting waste uranyl remobilization, as well as in developing more effective methods to retain uranium captured from aqueous environments.

2.2 Introduction

Uranium (U), in the form of uranyl ions (UO_2^{2+}), can be present as a radiological contaminant in surface and surface environmental systems (e.g., groundwater). Typical sources include coal power plant emissions, leachate from uranium ore mining, and degraded radioactive waste from both military and civilian sources, all of which pose potential contamination risks to local ecology and water sources for human consumption.[1] Exposure to this persistent, mobile toxin has been found to induce long-lasting detrimental effects to humans.[2,3] Legacy radioactive waste storage facilities at sites across the world, e.g., the U.S. DOE Hanford site, have exceeded their planned life expectancy and have been shown to leak into their surrounding environment.[4,5] An approach for legacy and modern high-level wastes (HLW) and Intermediate-level wastes (ILW) is solidification with inert species (e.g., vitrification) and storage within steel containers, where the radioactive elements will decay over timescales of hundreds of years to millennia.[5,6] Multiple layers of containment further protect this solidified waste from external perturbations, although self-induced and environmentally-driven corrosion and eventual leakage remain a challenge and a risk.[5–8] It is imperative that said waste remains unperturbed for millennia (e.g., within a geological storage facility), allowing the contained radioisotopes to decay.

Engineered materials, such as steel linings used to contain radioactive waste, may gradually corrode, and transform to environmentally ubiquitous and stable iron oxides (e.g., hematite and goethite). Depending on environmental conditions, a variety of iron oxide and oxyhydroxide polymorphs can form.[9] Hematite (α-Fe_2O_3) is stable in a wide range of geologic conditions. Hematite nanoparticles have been shown to be highly effective at adsorbing aqueous heavy metals and actinides.[10–13] Its high adsorptive performance enables its effectiveness in water remediation against toxic heavy metal ions. It has been well-established that aqueous uranium may become immobilized by iron oxide polymorphs by a combination of adsorption on the surface and incorporation within the structure of these nanoparticles.[14–16] While surface sorption may be effective in retarding of aqueous uranium migration in the sub surface, changes in surrounding environment (e.g., pH) or favorable adsorption of competing species may remobilize uranium.[17] Kinetic and structural studies have demonstrated additional pathways where uranium is more strongly retained within the rhombohedral structure of α-Fe_2O_3.[10,16,18–20] Understanding this behavior is paramount to understand the role and significance of iron oxides immobilizing radionuclide leachate in future geological disposal environments, as well as the efficacy of iron oxides as a long-term capture and storage medium for uranium from contaminated effluents.

The ability of α-Fe_2O_3 to structurally incorporate uranium, rather than only surface adsorb, provides a promising secondary uranium immobilization pathway. The coordination environment of the more strongly restrained uranium has been studied for a variety of iron oxide polymorphs prevalent in differing environmental conditions. Research has generally shown hematite to incorporate U within its Fe sites during its transformation from colloidal ferrihydrite, where U is surrounded by distorted O octahedra and neighboring Fe sites.[16,19–21] However, it is not yet understood how stability (thermodynamic and/or kinetic) scales with incorporation capacity within each polymorph. Conflicting interpretations from such studies propose different charge compensation schemes point to different proposed local Fe vacancy configurations. The differences in potential energy of each configuration have been calculated, but experimental findings have not necessarily agreed with the lowest energy configurations. For example, a *trans*-corner Fe vacancy configuration surrounding U sites has been proposed, despite having a 112 kJ/mol energy penalty relative to single face-sharing and dual edge-sharing vacancy configurations.[22] These localized energy calculations do not necessarily scale or represent the energetics of the bulk oxide, and data on the formation enthalpy of U-incorporated iron oxides is not yet known. Collecting such measurements will reveal the thermodynamic consequences of incorporation as a function of U content within the solid. The ability to retain the captured actinide under geological time scales relevant to radioactive waste storage requires further research.

Our key objective is to explore the effects of uranium incorporation on the thermodynamic stability of hematite. We describe herein, the hydrothermal synthesis of hematite nanoparticles from precursor Fe(III) and U(VI) salts, defined as α-$U_xFe_{2-2x}O_3$. . Extended X-ray absorption fine structure (EXAFS) was performed to explore local U coordination to validate structural incorporation and describe local U coordination. The effect of this structural incorporation on standard formation enthalpies of single-phase samples was measured using high temperature oxide melt solution calorimetry. Determining their formation enthalpies relative to mixtures of iron and uranium oxides may constrain stability of uranium retention over geologic timescales. These complementary techniques provide insight to the stability and effectiveness of iron oxides for radionuclide immobilization. Results from this research provide new perspectives on the effectiveness of iron oxides under environmental and engineered conditions to sequester uranium.

2.3 Experimental Methods

2.3.1 Synthesis

Synthesis of uranium-incorporated hematite (α-$U_xFe_{2-2x}O_3$) has been achieved by mixing $Fe(NO_3)_3·9H_2O$ (Sigma-Aldrich, ACS Reagent ≥ 98 %) and $UO_2(NO_3)_2·9H_2O$ (JT Baker, 'Baker Analyzed' Reagent) in 18.2 MΩ·cm deionized water. A total of 7 uranium-loaded samples were synthesized for calorimetric measurements. Uranyl concentrations ranged from 0.28 – 5.25 mM, while maintaining Fe(III) at 41 mM. 5 N NaOH (Fisher Scientific, Certified ACS) was used to titrate the acidic solution up to pH 7 ~ 9 while stirring at room temperature. Formation of colloidal ferrihydrite was observed around pH 5.6, at which point the precipitate was expected to favorably adsorb the uranyl species.

Hydrothermal treatment was used to accelerate the full transformation from ferrihydrite to hematite, preventing secondary phases (e.g., goethite, α-FeOOH) from otherwise forming.[9] 120 mL of the colloidal suspension was transferred to a 200 mL Teflon-lined hydrothermal vessel from Parr Instrument Co. The vessel was then sealed and placed into an oven at 180 °C for 24 to 72 hours, followed by gradual cooling in air.

The product was fully transformed into α-Fe_2O_3 and was collected at the bottom of the vessel. Aliquots of the supernatant were preserved for elemental concentration analysis, which was used to determine uranyl concentration in solution after synthesis. The precipitate was washed multiple times with DI water while agitating to remove residual salts, followed by centrifugation to collect the nanoparticles. The reaction for producing the final product is reported as **Eqn. 2.1**:

$$\boldsymbol{x(UO_2)^{2+}{}_{(aq)} + (2-2x)Fe^{3+}{}_{(aq)} + (3-2x)H_2O_{(l)} \xrightarrow{180\,^{\circ}C} U_xFe_{2-2x}O_{3(s)} + (6-4x)H^{+}{}_{(aq)}} \qquad \textbf{(2.1)}$$

This study focused on the stability of uranium well-immobilized within hematite particles, absent of surface-bound uranyl and colloidal uranium-containing impurities. Additional washing steps using a solution of HCl below pH 2.5 were performed to achieve this, removing weakly retained uranium (e.g., surface adsorbed).[23,24] Subsequent water washes were performed to clean and neutralize the product. Sample was then dispersed in ethanol and dried in air at 80 °C overnight.

2.3.2 Structural and Electronic Characterization

Identification of the desired iron oxide phase, and the absence of undesired secondary phases, is imperative for properly analyzing calorimetric data. Powder X-ray diffraction (PXRD) of the final product was performed to validate phase purity and crystallinity (Bruker D8 Advance, Cu K-α_I). Transmission electron microscopy (TEM) was performed to validate phase purity shown by XRD, as well assess uranium distribution within the iron oxide crystallites.[19] Imaging was performed using a JEOL 2100F at 200kV and FEI Tecnai F30 at 300 kV, both in STEM mode.

Samples were prepared by dispersing and sonicating powders in IPA and drop-cast onto carbon-backed Cu mesh grids. The grids were then baked out overnight at 80 °C and plasma-cleaned prior to imaging.

The coordination environments of uranium retained within hematite were determined by X-ray absorption spectroscopy (XAS) data of U spectra. Uranium L_{III}-edge (17.1663 keV) spectra were collected on beamline B-18, Diamond Light Source (DLS), under liquid nitrogen in fluorescence mode. Individual scans were calibrated with inline yttrium foil reference spectra, then merged to maximize the signal-to-noise ratio for the sample.

2.3.3 Stoichiometry Determination

Thermogravimetric analysis (TGA) was performed in parallel with differential scanning calorimetry (DSC) using a Setaram Labsys Evo. Powders were pressed into pellets of 10-20mg and placed in a 100 µL platinum crucible. Samples were heated from 25 to ≥ 800 °C at 10 °C/min while flushing the chamber with O_2. TGA quantified the amount of water adsorbed onto U-hematite particles. DSC data showed heat effects from dehydration and screened for other potential reactions induced by heating. A suitable drying temperature was selected based on these data. Uranium-free hematite analogues were then degassed under rough vacuum at 250 °C for 24 hours. Surface areas of these analogues were determined using Brunauer-Emmett-Teller (BET) N_2 adsorption (Micromeritics Gemini VII 2390). Surface areas of U-free powders analogous to U-loaded samples averaged 15.05 ± 0.08 m^2/g, or 2403.30 ± 13.20 m^2/mol. Solid samples were digested in 5 N HCl at 90 °C then diluted to 2 % HCl for inductively coupled plasma mass spectrometry (ICP-MS) analysis. Molar ratios of each element were then used to calculate the U/Fe stoichiometry of anhydrous product, defined as α-$U_xFe_{2-x}O_3$.

The differences in uranium content between the starting amount, amount remaining in solution after synthesis, and amount retained in the collected final product, were then used to calculate the amount of uranium lost to the successive washing and acid-leaching procedures. Lost uranium here is considered a combination of uranyl species adsorbed to hematite surfaces, poorly crystalline uranium-containing colloids, and losses from repeated washing and centrifugation steps. At the same time, Fe concentrations validated that all the introduced Fe(III) had precipitated by the end of the reaction.

2.3.4 Calorimetry

High temperature oxide melt solution calorimetry was performed using a custom-built twin calvet calorimeter held at 700 °C with molten sodium molybdate ($3Na_2O{\cdot}4MoO_3$) as the solvent. Approximately ≤ 7 mg of sample was pelletized and dropped into the melt for each of multiple measurements. Oxygen gas was flushed above the solvent at 51.6 mL/min and bubbled through it at 5.9 mL/min. Doing so maintained a consistent atmosphere above the molten solvent, while also mechanically mixing and accelerating dissolution of samples. The enthalpy of dissolution (ΔH_{ds}) was calculated by integrating the measured heat flow from dissolving the powder over time. This value was then used to calculate the standard formation enthalpy of the material. Measurements with the calorimeter were calibrated against bulk α-Al_2O_3 powder, which yield heat effects of comparable magnitude.

2.4 Results and Discussion

2.4.1 Synthesis and Characterization of α-$U_xFe_{2-x}O_3$

XRD patterns reveal consistent production of crystalline hematite nanoparticles (**Figure 2.1**). Each diffraction peak matched those of standard hematite,[25] with diffraction peak-broadening characteristic of nanoscale crystals. Furthermore, diffraction patterns suggest the absence of any uranium-bearing minerals in the acid-washed powders, possibly resulting from homogeneous UO_x distribution and low total U content. Whole-pattern Rietveld refinement (MDI Jade 6) of pristine powders suggested typical crystallite diameters of 25 – 90 nm.

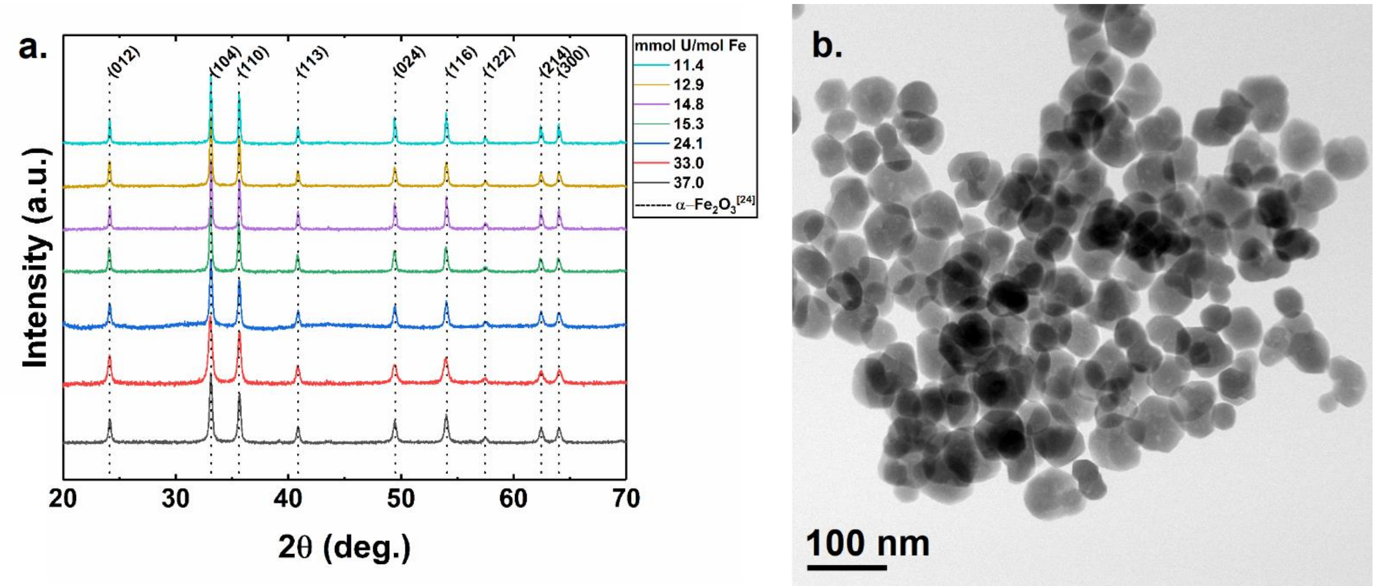

Figure 2.1 XRD patterns acquired of single-phase hematite, coprecipitated with varying initial concentrations of uranyl ions (**a**) and representative bright field TEM micrograph of crystalline hematite nanoparticles (**b**).

TEM corroborated findings by XRD that synthesized materials were single-phase crystalline nanoparticles, without any uranium-bearing colloids or secondary iron oxide phases (**Figure 2.2**). The stark Z contrast of U relative to Fe and O in HAADF micrographs revealed that U is well distributed throughout individual nanocrystals, as well as along grain boundaries of aggregated nanoparticles (**Figure 2.2**). Uranium was not concentrated along particle circumferences, suggesting surface-bound uranium species were desorbed, and observable U had been recalcitrant to acid washing. Evenly distributed U, as observed by EDS, further validated the hypothesis that uranium may homogenously persist throughout – in addition to clustering along the grain boundaries (**Appendix A, Figure SI-1, SI-2**). Results from subsequent characterization were then attributable to incorporated uranium and not convoluted by external uranium-bearing species.

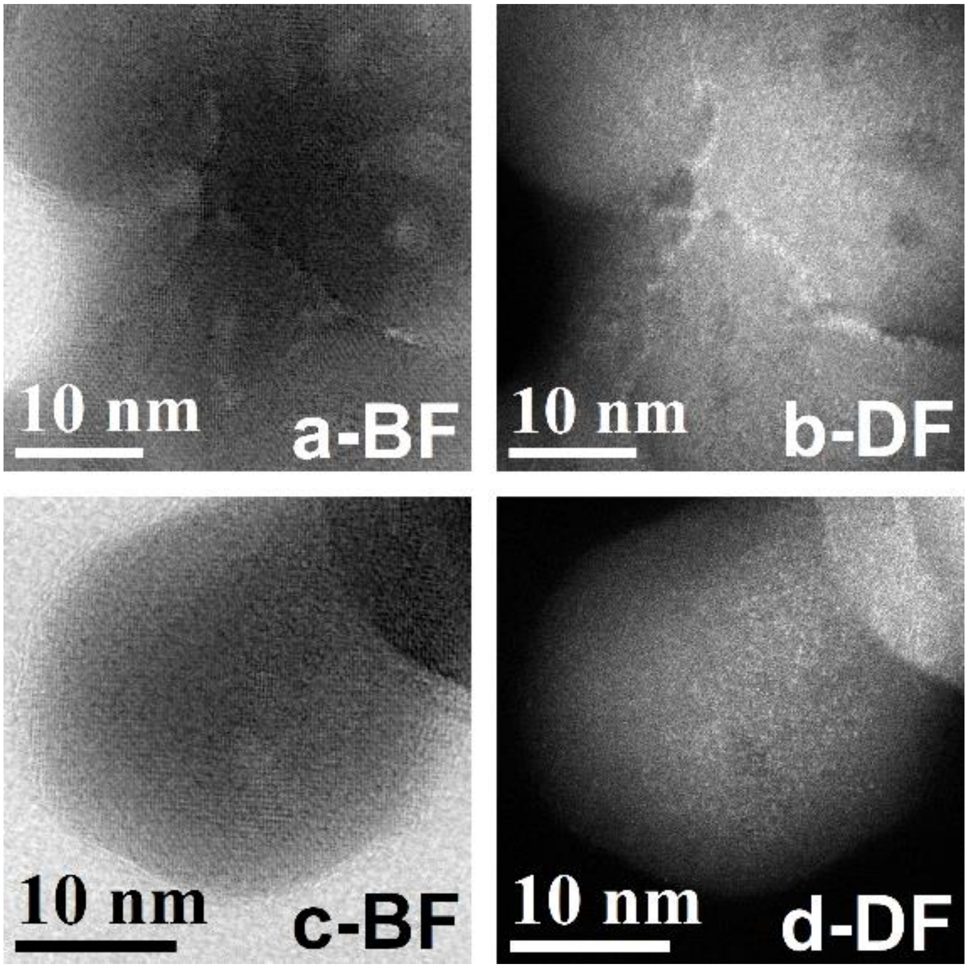

Figure 2.2 Brightfield (**BF**) and HAADF (**DF**) TEM micrographs of uranium largely collected along hematite grain boundaries (**a**, **b**) and uranium evenly distributed along lattice fringes (**c**, **d**).

2.4.2 Uranium Coordination

Considering the phase purity of synthesized samples, we attribute our U-O spectra of $U_{0.033}Fe_{1.934}O_3$ to those retained within hematite, as opposed to any potential goethite or surface uranyl that may otherwise have been present. EXAFS fits of U L_{III}-edge spectra reveal that the axial oxygen bonds characteristic of uranyl is retained after hydrothermal induction into hematite, albeit with minor elongation relative to those referenced in liebigite.[26] This calculated uranyl-like length of 1.79 Å matches that found by Ilton et al., and is considerably shorter than what was reported by Marshall et al. (1.87 Å).[19,21] The four equatorial oxygen atoms are bound slightly longer than lengths seen within standard oxygen atoms surrounding Fe sites (**Table 1, ΔR**), likely due to the large size difference of U^{6+} (0.870 Å) compared to Fe^{3+} (0.785 Å).[27]

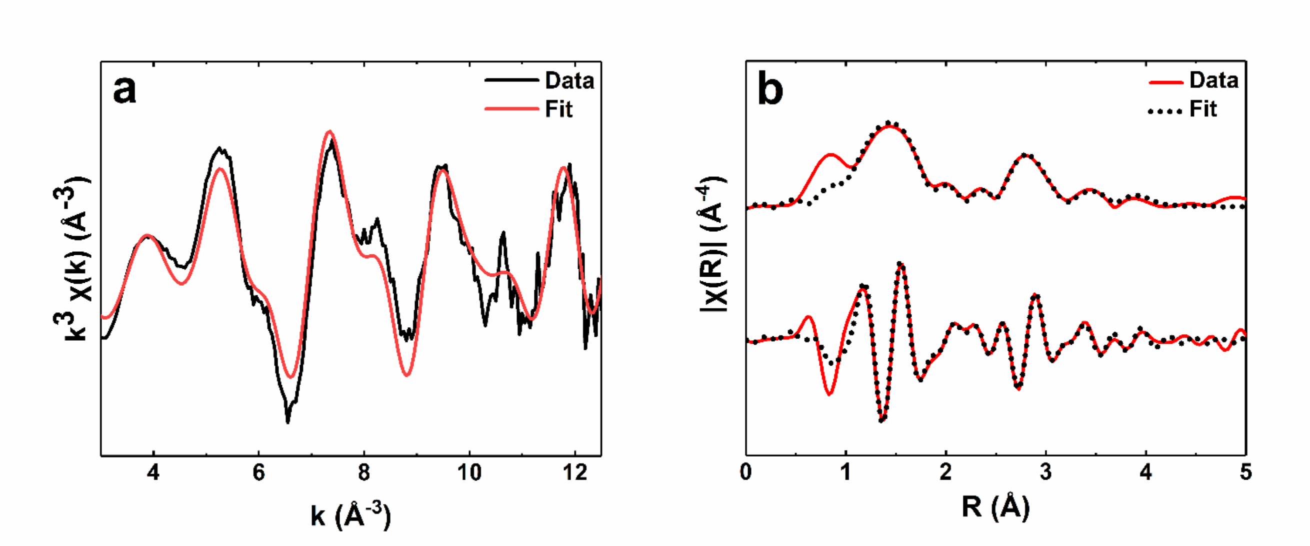

Figure 2.3 Uranium L_{III}-edge EXAFS spectra (a) and Fourier transform (b) from U(VI)-incorporated hematite, $U_{0.033}Fe_{1.934}O_3$.

Table 2.1 EXAFS fit results demonstrating uranium incorporation within $U_{0.033}Fe_{1.934}O_3$ (t = 24 hours, 180 °C), using a k-range of 3.0 – 12.2.

U-path	CN	R_{ref} (Å)[24,26]	R_{lit} (Å)[21]	**R (Å)**	ΔR (Å)	σ^2 (Å^2)	ΔE_0 (eV)	$S0^2$	χ_v^2	R_{fit}
O_{Axial}	1.9	1.77(9)	1.87(2)	**1.79(4)**	0.01(5)	0.006(4)	-3.0 ± 1.9	1	152.7	0.0195
$O_{Equitorial-1}$	2.2	1.94(6)	2.07(2)	**2.07(6)**	0.13(0)	0.010(1)				
$O_{Equitorial-2}$	1.9	2.11(6)	2.23(3)	**2.21(4)**	0.09(8)	0.010(1)				
Fe_{Edge}	2.8	2.97(1)	3.11(2)	**3.09(1)**	0.12(0)	0.006(9)				
$Fe_{Corner-1}$	2.0	3.36(4)	3.45(6)	**3.27(4)**	-0.09(0)	0.007(2)				
$Fe_{Corner-2}$	2.0	3.70(5)	4.01(6)	**3.50(4)**	-0.20(1)	0.010(7)				
Fe_{Cell2}	1.0	3.98(6)	--	**4.11(5)**	0.12(9)	0.010(7)				
Fe_{Face}	--	2.90	2.87(3)	**--**	--	--				
	CN – coordination number R – atomic distance ΔR – difference from reference values σ^2 – Debye-Waller factor ΔE_0 – energy shift from U L_{III} $S0^2$ – amplitude factor χ_v^2 – reduced χ square value R_{fit} – goodness of fit									

EXAFS results reveal coordination to multiple neighboring iron sites, which serves as evidence of structural incorporation and occupation of iron sites within the hematite lattice (**Figures 2.3-2.4, Table 2.1**). U-Fe shells were resolved up to 4.11 Å, most notably with the absence of the face-sharing (nearest neighboring; 2.90 Å) Fe shell. This finding is partially corroborated by AIMD calculations of vacancy configurations for U in hematite by McBriarty et al., where the single face-sharing vacancy results in the lowest energy structure.[22] However, this conflicts with conclusions by them and others that charge compensation is accomplished by two opposing corner-sharing vacancies – despite being the highest calculated energy (least favorable) configuration.

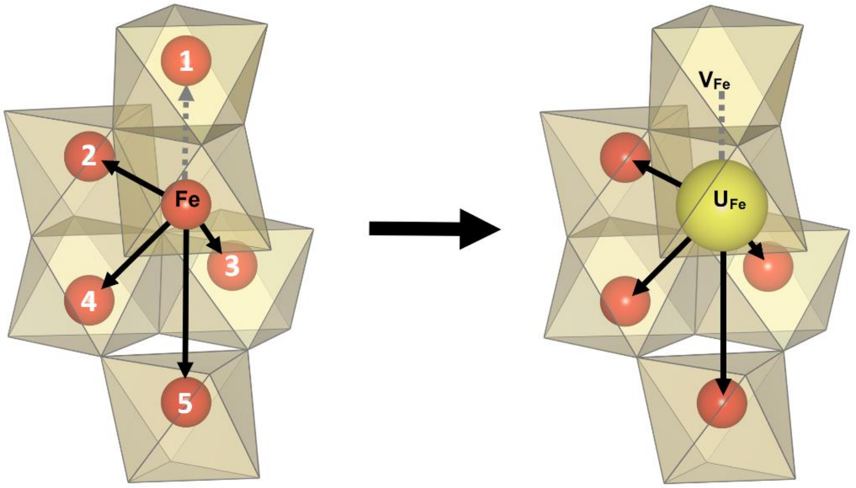

	ΔR (Å)
1	--
2	+0.12(0)
3	-0.09(0)
4	-0.20(1)
5	+ 0.12(9)

Figure 2.4 Effects of U-Fe substitution on local coordination within hematite structure, as calculated from U L_{III} EXAFS. Calculated distances are compared to literature results in **Table 2.1**.

Acquired EXAFS data partially agree with existing literature on uranium-incorporated hematite, in that uranium substitutes for Fe within the hematite structure. Differences in interpretations primarily revolve around U-Fe shells and vacancy formation. An earlier study by Marshall et al. found the face-sharing site to be present and with a shorter U-Fe distance (2.87 Å) than its standard Fe-Fe length (2.90 Å).[21] Other U-Fe shells appear in agreement, although the outermost shell had not previously been resolved. U-O coordination between the two studies agree, with two uranyl-like axial bonds and 4 hematite-like equatorial bonds. Meanwhile, a*b initio*-guided EXAFS work by McBriarty et al. determined iron vacancy formation at opposing corners (2C) from the central uranium site.[20] This fit best with their EXAFS data, despite being the highest calculated energy configuration. By contrast, our result of a single face-sharing vacancy (F) agrees with their lowest energy configuration. They report the 2C configuration to best fit their EXAFS data, although comparisons were shown for 2C+F rather than F alone. Later studies by Ilton et al. found that vacancies at *trans*-corner and face-sharing sites may form.[28] It is possible that these conflicting conclusions are all valid. The specific coordination environment of U within hematite may be highly sensitive to differences in environmental conditions and incorporation processes.

Including the face-sharing shell significantly worsened the EXAFS fit in our study. Meanwhile, F-tests showed high confidence of its absence, as opposed to all other Fe shells being present (including corner-sharing sites) with high confidence (**Appendix A, Table SI-1, SI-2**).[29] The Fe site 2.90 Å from the central atom is consistently absent and serves as the charge compensation mechanism for U(VI) occupying an Fe(III) site. This site was closest and most subject to strain from the adjacent U atom. Presumably, forming this vacant site alleviated the strain and distortion induced by U-Fe substitution. The innermost and outermost resolved U-Fe shells expanded relative to reference hematite bond lengths, whereas the intermediate length sites contracted.

Observed differences in local U coordination may result from a variety of experimental conditions. Our study used single-phase samples, which prevented convoluting our findings with those of goethite. Formation of the face-sharing vacancy configuration may be unique to hematite formation at elevated temperatures (e.g., 180 °C), and it is unclear if the same may be observed at the lower temperatures seen in other studies. Our results indicate that uranium enters and is stabilized within the hematite structure, all while maintaining the uranyl-like coordination of the axial oxygen bonds. Uranium was bound into distorted oxygen octahedra, comparable to local environments of U^{6+} in hematite such as described by Marshall et al.[21] Considering the similarities in EXAFS spectra among existing literature, it may be presumed that our hydrothermal synthesis conditions do not severely alter the coordination environments from those resulting from ageing under ambient conditions.

We postulate that thermodynamic trends from this study is applicable to similar structural studies in which uranium is well-retained within hematite nanoparticles. Less directly applicable are specific thermodynamic values at given uranium concentrations. For studies where higher-energy vacancy configurations are found (e.g., 2C), it is possible that the overall formation enthalpy is consequently shifted upwards (less stable/more metastable). However, the significance of this potential difference is unknown. Results on the energetics of these samples are discussed further below.

2.4.3 Stoichiometry - Dehydration

Quantifying the extent of hydration per unit of solid is needed to account for its contribution to calorimetric results. Water-corrected enthalpy measurements ($\Delta H_{\text{ds-H2O, 700 °C}}$) are reported in **Table 2.2**. Representative TGA and DSC traces are shown in **Appendix A, Figure SI-4**. Despite having been dried at 80 °C for over 12 hours, the small particle size and corresponding high surface area are able to retain considerable amounts of water. Water content from TGA ranged between 0.025 – 0.030 mol H_2O/mol Fe_2O_3. Most water was released around 100 °C, while the more strongly chemisorbed water required higher temperatures to detach from the nanoparticle surfaces. DSC curves consistently revealed the onset of an endothermic trend near 290 °C with no inflection in the TGA slope. This finding suggests only a structural change at elevated temperatures, possibly due to aggregation of the nanoparticles when still slightly hydrated.

2.4.4 Stoichiometry - Uranium Remobilization and Retention Pathways

Uranium concentrations within solid hematite samples were calculated from ICP-MS of acid-digested solids and are reported in **Table 2.2**. A range of 1.1 – 3.7 mol % U was incorporated in our samples, representing a 2 to 5-fold increase from 0.6 – 0.7 mol % U samples explored in previous studies.[16,19,21,22,28] Additionally, the supernatant from five samples after hydrothermal treatment were evaluated to confirm that negligible amounts of uranium and iron remained in solution. This finding shows that all the uranium and iron had effectively been immobilized. Mass balance calculations were then used with ICP-MS data to determine the amount of uranium that had been weakly adsorbed to precipitate surfaces, coprecipitated into acid-unstable (< pH 2.5) solids, and strongly incorporated within hematite particles (final product). The relative amounts of uranium partitioned to each pathway are shown as a function of initial uranyl concentration in **Figure 2.5**. ICP-MS results also revealed that uranium loading within hematite increased at higher uranyl concentrations. However, a smaller proportion of total U(VI) becomes incorporated, with the remainder favorably adsorbing or coprecipitating outside of the hematite particles.

Uranium immobilization pathways under hydrothermal conditions may vary depending on treatment duration and initial uranyl concentrations. A smaller thermodynamic penalty (further discussed below) was observed for samples with shorter treatment times (**Figure 2.6**). This is speculated to result from kinetic limitations, where even 72 hours may not have been long enough to reach equilibrium in the vessel at 180 °C. Extended hydrothermal treatment facilitates uranium mobilization throughout the iron oxide lattice, though at an appreciable energetic penalty. The kinetics of uranium immobilization by this technique may be elucidated by exploring lengthier time periods and a wider range of hydrothermal conditions. This finding may shed light towards exploiting and optimizing iron oxide nanoparticles for capture and storage of aqueous uranium leachate.

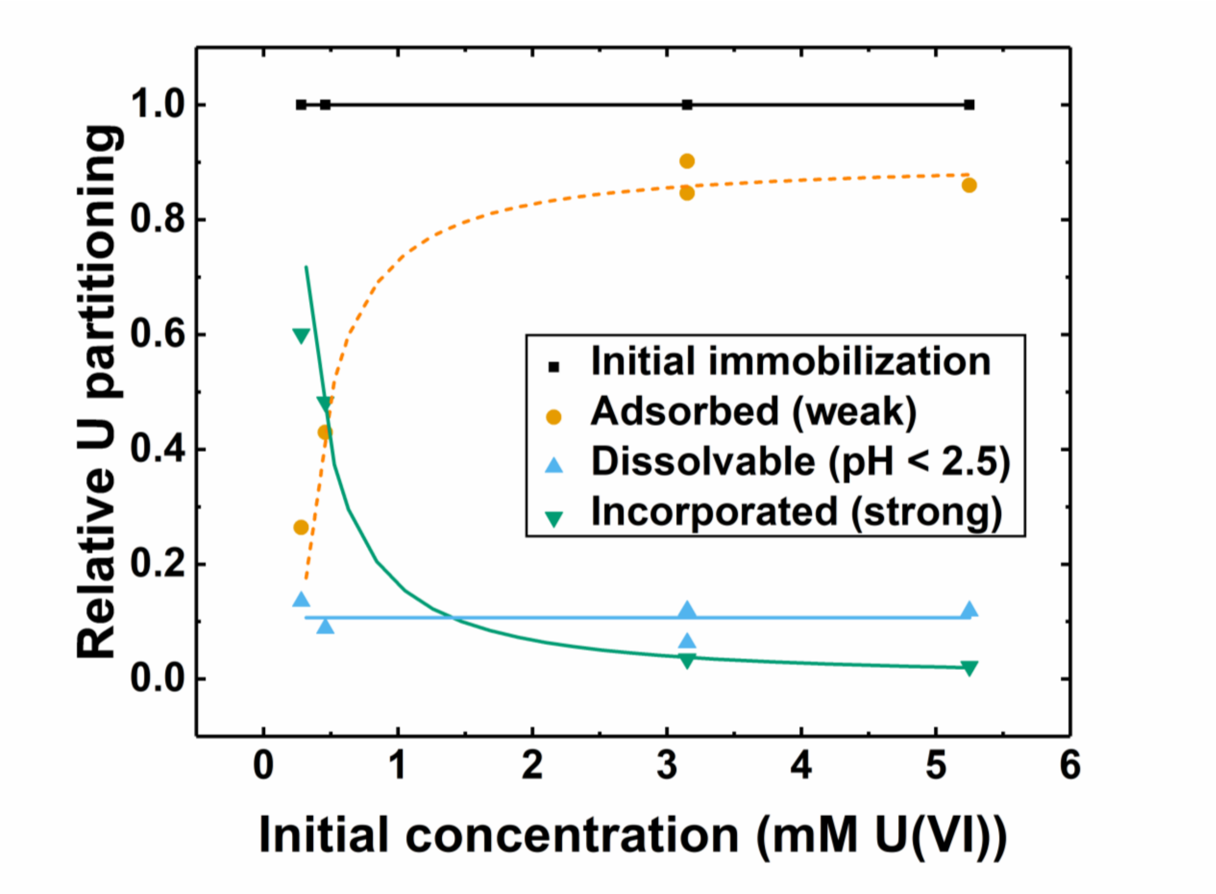

Figure 2.5 Effect of U_0 on uranium partitioning to immobilization pathways, based on ICP-MS calculations and shown as fractions of total uranium in system.

The relative favorability of each retention pathway may be seen in **Figure 2.5**. With increasing uranyl concentrations, the immobilization pathways by which hematite retains uranium would shift dramatically. While all aqueous uranium was captured from each tested synthesis condition, the most favorable route at lower uranyl concentrations was incorporation. Uranium incorporation became progressively more challenging to achieve with higher uranium concentrations in solution.

Possibly more important in dictating concentration of well-incorporated U is reaction time. Samples subjected to elevated temperatures for 24 hours tended to result in lower U loadings than those held for 72 hours (**Table 2.2, Figure 2.6**). This is hypothesized to highlight the practical differences in incorporated uranium collection primarily along grain boundaries compared to homogeneous lattice substitution.

2.4.5 Energetics of Uranium Incorporation

To determine the formation enthalpies of the oxides themselves, hydration contributions needed to be removed. As determined by TGA, each sample retained quantified amounts of adsorbed water. Bulk water contributions at 700 °C were approximated as 69.0 kJ/mol H_2O and subtracted from measured values.[30] Water corrected measurements were reported as ΔH_{ds} and used for subsequent thermodynamic calculations. A summary of uranium concentrations and corresponding thermodynamic values are provided in **Table 2.2**.

Decreased stability from high surface areas contributed to measured calorimetric values of nanoparticles. Nanoscale α-Fe_2O_3 has been reported to have a surface energy of 1.9 ± 0.3 J/m^2**.**[31] BET surface areas from analogous uranium-free powders averaged 2403.3 ± 13.2 m^2/mol and are assumed to be comparable to those for uranium-loaded samples. Our reference point for measured calorimetric values was a uranium-free hematite of comparable surface area. In doing so, surface energetics of nanoparticles are removed from enthalpy calculations relative to binary oxides.[32]

Table 2.2 Measured and calculated thermodynamic properties for $U_xFe_{2-2x}O_3$. $\Delta H°_{f,ox}$ is calculated as standard formation enthalpy of the mixed oxide relative to the weighted values for α-Fe_2O_3 and γ-UO_3.

x (mol U)	n (mol H_2O)	[U_0] (mM)	t_{rxn} (hr)	$\Delta H_{ds,\ 700\ °C}$ (kJ/mol)	$\Delta H_{ds\text{-}H_2O,\ 700\ °C}$ (kJ/mol)	$\Delta H°_{f,el}$ (kJ/mol)	$\Delta H°_{f,ox}$ (kJ/mol)
0.000(0)	0.000	0.00	24	91.06 ± 0.88	91.06 ± 0.88	-821.63 ± 2.39	4.57 ± 1.83
0.013(0)	0.417	0.28	24	99.47 ± 1.28	70.74 ± 1.28	-807.57 ± 2.56	23.77 ± 2.06
0.015(3)	0.264	3.15	24	88.13 ± 1.08	69.92 ± 1.08	-807.88 ± 2.47	24.40 ± 1.94
0.033(0)	0.488	5.25	24	90.86 ± 0.73	57.19 ± 0.73	-803.73 ± 2.34	35.59 ± 1.77
0.011(5)	0.222	0.28	72	87.66 ± 1.32	72.32 ± 1.32	-808.43 ± 2.58	22.33 ± 2.08
0.014(8)	0.228	0.46	72	89.11 ± 0.75	73.42 ± 0.75	-811.16 ± 2.34	20.94 ± 1.78
0.024(1)	0.199	3.15	72	68.13 ± 1.19	54.41 ± 1.19	-796.66 ± 2.52	39.14 ± 2.00
0.037(0)	0.219	5.25	72	38.87 ± 2.69	23.77± 2.69	-772.26 ± 3.49	68.67 ± 3.13

n – excess water bound by chemisorption and physisorption
[U_0] – initial uranyl concentration
t_{txn} – hydrothermal treatment time
$\Delta H_{ds,\ 700°C}$ – measured enthalpy of drop solution
$\Delta H_{ds\text{-}H_2O,\ 700°C}$ – water-corrected enthalpy of drop solution
$\Delta H°_{f,el}$ – standard formation enthalpy relative to constituent elements
$\Delta H°_{f,ox}$ – standard formation enthalpy relative to binary oxides

Formation enthalpies with any amount of uranium indicate metastability relative to separate binary oxides (α-Fe_2O_3 and UO_x) (**Table 2.2, $\Delta H°_{f,ox}$**). With increasing uranium concentration, the energetic stability of the composite oxide decreases relative those of its binary oxide constituents. Relative to binary oxides, structural incorporation increases (makes less exothermic) the formation enthalpy of the mixed oxide. At the higher concentrations of well-retained uranium, the overall energetic stability of 24-hour samples is greater than that of 72-hour samples. In both cases, entropic contributions facilitate this incorporation behavior. Meanwhile, the extent to which incorporation occurs is kinetically limited, as suggested by the 5.25 mM U(VI) starting solution retaining more U in the final solid after 72 hours (3.7 mol % U) rather than 24 hours (3.3 mol % U). It may be relevant to consider that extended hydrothermal treatment times typically allow nanoparticles to fully crystallize, aggregate, grow, and ultimately stabilize.[23] If contaminated with aqueous uranyl species under such conditions, adsorbed uranium atoms are provided the opportunity to favorably diffuse into the iron oxide lattice. We therefore hypothesize that accelerated diffusion kinetics and expansion of the host lattice under elevated synthesis temperatures enables gradual uranium migration into Fe sites.

Table 2.3 Thermochemical reactions used to calculate standard formation enthalpies

	Reactions - Enthalpy of formation of $U_xFe_{2-2x}O_3$ from elements and from oxides at 25°C	Enthalpy, ΔH (kJ/mol)	
1	$\boldsymbol{U_xFe_{2-2x}O_{3(s,25°C)} \rightarrow (1-x)Fe_2O_{3(sln,700°C)} + xUO_{3(sln,700°C)}}$ **for** $\boldsymbol{0 < x < 0.037}$	$\boldsymbol{\Delta H_1 = \Delta H_{ds}}$	**Reference**
2	$\alpha - Fe_2O_{3(s,25°C)} \rightarrow Fe_2O_{3(sln,700°C)}$	$\Delta H_2 = 91.06 \pm 0.88$* (nano)	31,32
3a	$\gamma - UO_{3(s,25°C)} \rightarrow UO_{3(sln,700°C)}$	$\Delta H_{3a} = 9.49 \pm 1.53$	33
3b	$\frac{1}{3}U_3O_{8(s,25°C)} + \frac{1}{6}O_{2(g,25°C)} \rightarrow UO_{3(sln,700°C)}$	$\Delta H_{3b} = 54.0 \pm 6.4$	33
3c	$UO_{2(s,25°C)} + \frac{1}{2}O_{2(g,25°C)} \rightarrow UO_{3(sln,700°C)}$	$\Delta H_{3c} = -140.4 \pm 2.67$	33
4	$2Fe_{(s,25°C)} + \frac{3}{2}O_{2(g,25°C)} \rightarrow \alpha - Fe_2O_{3(s,25°C)}$	$\Delta H_4 = -826.2 \pm 1.3$	34
5	$U_{(s,25°C)} + \frac{3}{2}O_{2(g,25°C)} \rightarrow \gamma - UO_{3(s,25°C)}$	$\Delta H_5 = -1223.8 \pm 0.8$	34
6a	$(1-x)Fe_2O_{3(s,25°C)} + \boldsymbol{xUO_{3(s,25°C)}} \rightarrow U_xFe_{2-2x}O_{3(s,25°C)}$	$\Delta H_{6a} = \Delta H_{f,ox1}$	
6b	$(1-x)Fe_2O_{3(s,25°C)} + \boldsymbol{\frac{x}{3}U_3O_{8(s,25°C)}} + \frac{x}{6}O_{2(g,25°C)} \rightarrow U_xFe_{2-2x}O_{3(s,25°C)}$	$\Delta H_{6b} = \Delta H_{f,ox2}$	
6c	$(1-x)Fe_2O_{3(s,25°C)} + \boldsymbol{xUO_{2(s,25°C)}} + \frac{x}{2}O_{2(g,25°C)} \rightarrow U_xFe_{2-2x}O_{3(s,25°C)}$	$\Delta H_{6c} = \Delta H_{f,ox3}$	
7	$xU_{(s,25°C)} + (2-2x)Fe_{(s,25°C)} + \frac{3+y}{2}O_{2(g,25°C)} \rightarrow U_xFe_{2-2x}O_{3(s,25°C)}$	$\Delta H_7 = \Delta H_{f,el}$	

*Corrected from bulk to nanoscale (2403 m^2/mol) with 4.57 kJ/mol surface energy

$$\Delta H_{f,ox1} = -\Delta H_1 + (1-x)\,\Delta H_2 + x\,\Delta H_{3a}$$
$$\Delta H_{f,ox2} = -\Delta H_1 + (1-x)\,\Delta H_2 + x\,\Delta H_{3b}$$
$$\Delta H_{f,ox3} = -\Delta H_1 + (1-x)\,\Delta H_2 + x\,\Delta H_{3c}$$
$$\Delta H_{f,el} = -\Delta H_1 + (1-x)\,\Delta H_2 + x\,\Delta H_3 + (1-x)\,\Delta H_4 + x\,\Delta H_5$$

for $0 < x < 0.037$

Uranium may be well retained through two routes within hematite nanoparticles. As evidenced by TEM, uranium atoms may cluster along the boundaries of hematite aggregates and along hematite lattice fringes (**Figure 2.2b)**. In addition, EXAFS interpretations confirm uranium can occupy iron sites throughout the host structure. Modifying the favorability of each pathway may be achieved by modulating hydrothermal reaction times. Enthalpic trends for different reaction times are shown as functions of initial uranyl concentrations in **Figure 2.6**. Formation of the 24-hour mixed oxides face a relatively minimal enthalpic penalty with increasing uranium content. We hypothesize the shorter reaction time to favor formation of α-Fe_2O_3 with UO_x clustering along its grain boundaries. An opposite thermodynamic trend was seen in samples synthesized for 72 hours, where increasing uranium concentration resulted in greater increases in formation enthalpies. This is expected to result from longer reaction times, facilitating increased U migration kinetics and greater U-Fe substitution. The differences resulting from varying hydrothermal treatment times also suggest that equilibrium had not been reached in these metastable oxides. As a result, entropy terms could not be calculated, and the roles incorporation kinetics and entropic contributions on the studied samples are unclear.

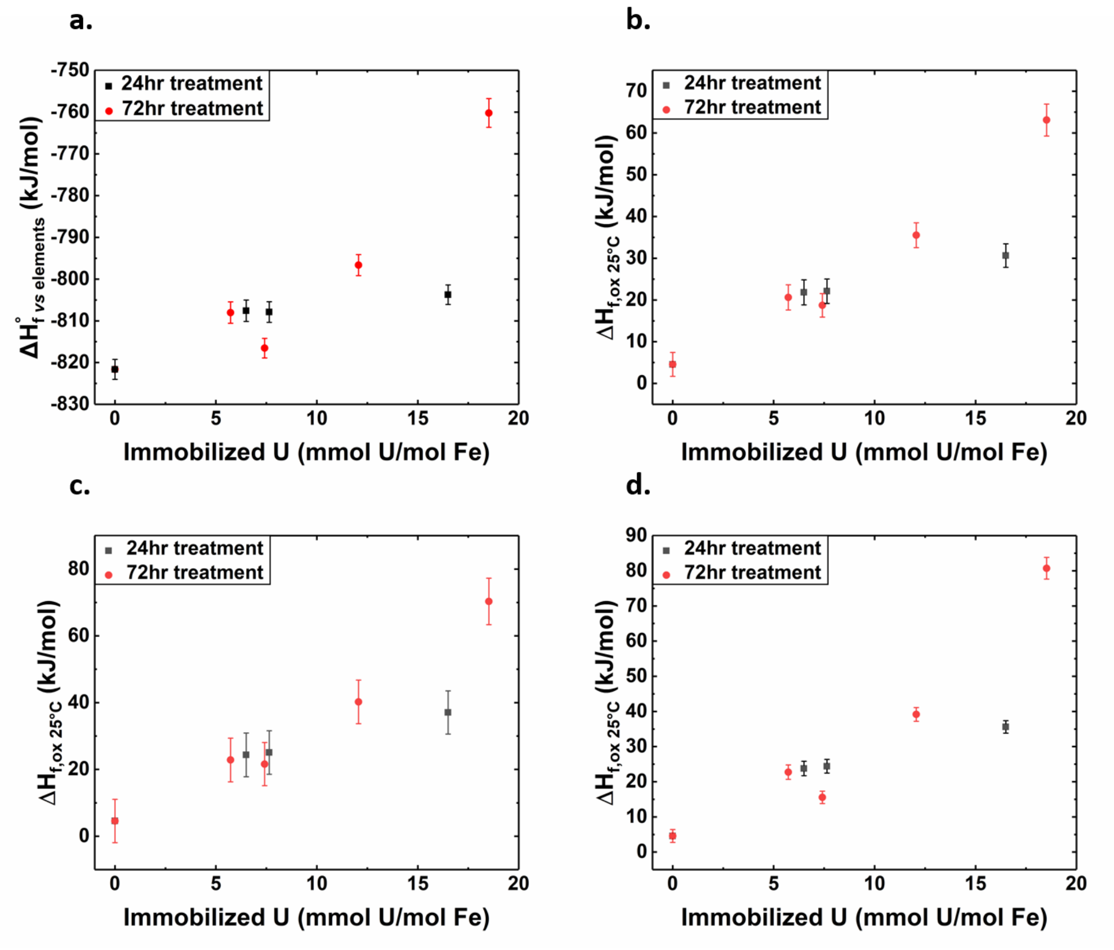

Figure 2.6 Formation enthalpy of uranium-incorporated α-Fe_2O_3 in relation to constituent elements (U, F, O) (**a**), binary oxides (UO_2, α-Fe_2O_3) (**b**), binary oxides (U_3O_8, α-Fe_2O_3) (**c**), binary oxides (UO_3, α-Fe_2O_3) (**d**).

Thermodynamic results reveal an interplay between maximizing uranium concentration within hematite (as an effective and efficient remediation medium) and maximizing energetic stability of the contained uranium. The characteristics of said interplay is heavily dependent on synthesis conditions, which dictate attribution to grain boundaries/solid solutions with uranium oxides or attribution to U_{Fe} substitution throughout nanoparticle lattices. Extended hydrothermal treatment times appear to allow uranium aggregates along grain boundaries to diffuse within the iron oxide lattice and remain trapped after cooling to ambient temperature. Shorter treatment times, meanwhile, favor higher relative concentrations along interfaces, and lattice-confined uranium may be primarily attributed to the initial co-precipitation of ferrihydrite and transformation to hematite. Reported formation enthalpies represent the stability of hematite with strongly bound uranium within its structure. However, quantitative distinctions in stability between pure lattice incorporation and pure grain boundary confinement have not been concluded. Our findings suggest a lower energy cost and higher stability with grain boundary confinement under circumneutral environments, at the cost of increased uranium remobilization potential under acidic conditions.

Results from this project provide data essential for understanding the fate of uranium in geological disposal sites over extended timescales and the transport of uranium in the environment. Identifying the stability of structural incorporation suggests the feasibility of iron oxides for inhibiting the mobility of leached uranium. Environmentally abundant iron-bearing minerals, and corrosion products from steel containment barriers for radioactive waste, may play a crucial role in inhibiting uranium species upon eventual leaching into the environment. These insights, including new thermodynamic data, will help guide the modeling and improvement of safe and scalable radioactive waste practices and water remediation applications, which ultimately improve water safety for humans and surrounding ecosystems.

2.5 Acknowledgements

This work was supported by the U.S. Department of Energy, Office of Basic Energy Sciences, grant DE-FG02-97ER14749 (Thermodynamics of Minerals Stable near Earth's Surface). Support was also provided by the Nuclear Regulatory Commission through the Advancing Scientific Careers to Enhance Nuclear Technologies (ASCENT) program. We also acknowledge the University of Manchester Department of Earth and Environmental Sciences and Diamond Light Source B18 Beamline for funding and facilitating EXAFS studies.

2.6 References

1. Chen, A., Shang, C., Shao, J., Zhang, J. & Huang, H. The application of iron-based technologies in uranium remediation: A review. *Sci. Total Environ.* **575**, 1291–1306 (2017).
2. Kurttio, P. *et al.* Renal effects of uranium in drinking water. *Environ. Health Perspect.* **110**, 337–342 (2002).
3. Orloff, K. G. *et al.* Human exposure to uranium in groundwater. *Environ. Res.* **94**, 319–326 (2004).
4. Peterson, R. A. *et al.* Review of the Scientific Understanding of Radioactive Waste at the U.S. DOE Hanford Site. *Environ. Sci. Technol.* **52**, 381–396 (2018).
5. *Final Review of the Study on Supplemental Treatment Approaches of Low-Activity Waste at the Hanford Nuclear Reservation*. *Final Review of the Study on Supplemental Treatment Approaches of Low-Activity Waste at the Hanford Nuclear Reservation* (2020). doi:10.17226/25710
6. Goel, A., McCloy, J. S., Pokorny, R. & Kruger, A. A. Challenges with vitrification of Hanford High-Level Waste (HLW) to borosilicate glass – An overview. *J. Non-Crystalline Solids X* **4**, 100033 (2019).
7. Wronkiewicz, D. J. Effects of Radionuclide Decay on Waste Glass Behaviour - A Critical Review. (1993).
8. Burns, W. G., Hughes, A. E., Marples, J. A. C., Nelson, R. S. & Stoneham, A. M. Effects of radiation on the leach rates of vitrified radioactive waste. *J. Nucl. Mater.* **107**, 245–270 (1982).
9. Cornell, R. M. & Schwertmann, U. The Iron Oxides. in *Iron Oxides in the Laboratary* **164**, 5–18 (Wiley-VCH Verlag GmbH, 2003).
10. Zeng, H., Singh, A. & Basak, S. Nanoscale size effects on uranium (VI) adsorption to hematite. *... Sci. Technol.* **43**, 1373–1378 (2009).
11. Shuibo, X. *et al.* Removal of uranium (VI) from aqueous solution by adsorption of hematite. *J. Environ. Radioact.* **100**, 162–166 (2009).
12. Ho, C. H. & Doern, D. C. The sorption of uranyl species on a hematite sol. *Can. J. Chem.* **63**, 1100–1104 (1985).
13. Phuengprasop, T., Sittiwong, J. & Unob, F. Removal of heavy metal ions by iron oxide coated sewage sludge. *J. Hazard. Mater.* **186**, 502–507 (2011).
14. Waite, T. D., Davis, J. A., Payne, T. E., Waychunas, G. A. & Xu, N. Uranium(VI) adsorption to ferrihydrite: Application of a surface complexation model. *Geochim.*

Cosmochim. Acta **58**, 5465–5478 (1994).

15. Ohnuki, T. *et al.* Change in Sorption Characteristics of Uranium during Crystallization of Amorphous Iron Minerals. *J. Nucl. Sci. Technol.* **34**, 1153–1158 (1997).

16. Duff, M. C., Coughlin, J. U. & Hunter, D. B. Uranium co-precipitation with iron oxide minerals. *Geochim. Cosmochim. Acta* **66**, 3533–3547 (2002).

17. Smith, K. S. Metal Sorption on Mineral Surfaces. in *The Environmental Geochemistry of Mineral Deposits* 161–182 (Society of Economic Geologists, 1997). doi:10.5382/Rev.06.07

18. Marshall, T. A. *et al.* Uranium fate during crystallization of magnetite from ferrihydrite in conditions relevant to the disposal of radioactive waste. *Mineral. Mag.* **79**, 1265–1274 (2015).

19. Ilton, E. S. *et al.* Reduction of U(VI) incorporated in the structure of hematite. *Environ. Sci. Technol.* **46**, 9428–9436 (2012).

20. McBriarty, M. E. *et al.* Iron Vacancies Accommodate Uranyl Incorporation into Hematite. *Environ. Sci. Technol.* **52**, 6282–6290 (2018).

21. Marshall, T. A. *et al.* Incorporation of Uranium into Hematite during Crystallization from Ferrihydrite. *Environ. Sci. Technol.* **48**, 3724–3731 (2014).

22. McBriarty, M. E. *et al.* Iron Vacancies Accommodate Uranyl Incorporation into Hematite. *Environ. Sci. Technol.* **52**, 6282–6290 (2018).

23. Hao, Y. & Teja, A. S. Continuous hydrothermal crystallization of α–Fe 2 O 3 and Co 3 O 4 nanoparticles. *J. Mater. Res.* **18**, 415–422 (2003).

24. Lam, U. T., Mammucari, R., Suzuki, K. & Foster, N. R. Processing of iron oxide nanoparticles by supercritical fluids. *Ind. Eng. Chem. Res.* **47**, 599–614 (2008).

25. Blake, R. L., HessevicK, R. E., Zoltai, T. & Finger, L. W. Refinement of the Hematite Structure. *Am. Mineral.* **51**, 123–129 (1966).

26. Mereiter, K. The crystal structure of Liebigite, Ca2UO2(CO3)3·~11H2O. *TMPM Tschermaks Mineral. und Petrogr. Mitteilungen* **30**, 277–288 (1982).

27. Shannon, R. D. Revised effective ionic radii and systematic studies of interatomic distances in halides and chalcogenides. *Acta Crystallogr. Sect. A* **32**, 751–767 (1976).

28. Ilton, E. S. *et al.* Using Atom Dynamics to Map the Defect Structure around an Impurity in Nano-Hematite. *J. Phys. Chem. Lett.* **11**, 10396–10400 (2020).

29. Downward, L., Booth, C. H., Lukens, W. W. & Bridges, F. A variation of the F-test for determining statistical relevance of particular parameters in EXAFS fits. in *AIP Conference Proceedings* (2007). doi:10.1063/1.2644450

30. Chase, M. W. NIST-JANAF Thermochemical Tables, 4th Ed. J. Phys. Chem. Ref. Data. 1998, Monograph 9(Part I and Part II). *Journal of Physical and Chemical Reference Data* **Monograph**, Part I&II (1998).

31. Navrotsky, A., Ma, C., Lilova, K. & Birkner, N. Nanophase Transition Metal Oxides Show Large Thermodynamically Driven Shifts in Oxidation-Reduction Equilibria. *Science (80-.).* **330**, 199–201 (2010).

32. Majzlan, J., Navrotsky, A. & Evans, B. J. Thermodynamics and crystal chemistry of the hematite-corundum solid solution and the FeAlO3 phase. *Phys. Chem. Miner.* **29**, 515–526 (2002).

33. Guo, X. *et al.* Thermodynamics of formation of coffinite, $USiO_4$. *Proc. Natl. Acad. Sci.* **112**, 6551–6555 (2015).

34. Richard A. Robie & Hemingway, B. S. Thermodynamic Properties of Minerals and Related Substances at 298.15 K and 1 bar (105 pascals) and at Higher Temperatures. *U.S. Geol. Surv.* (1995).

Chapter 3

Aerobic Synthesis and Thermodynamics of Uranium-Incorporated α-FeOOH Nanoparticles

3.1 Abstract

Goethite nanoparticles were synthesized with U(VI) in alkaline, oxic water through a coprecipitation and hydrothermal treatment process. XRD, TEM, and EXAFS analyses reveal that uranium may both aggregate along grain boundaries and occupy iron sites within goethite. Uranyl ions may cluster along the interfaces of nanorod goethite aggregates. The described synthesis method produces crystalline, single-phase iron oxyhydroxide nanoparticles without surface-bound uranyl complexes. The observed U-O coordination was not representative of naturally occurring processes facilitated by redox reactions in abiotic and biogenic anoxic environments. However, EXAFS revealed similar U and Fe coordination to existing studies of U-Fe substitution in goethite under anoxic environments and without Fe(II) as a catalyst for U(VI) reduction and goethite crystallization. This work provides and validates an alternative method of synthesizing uranium-immobilized goethite nanoparticles for further mechanistic studies. High temperature oxide melt solution calorimetry measurements were performed to calculate the thermodynamic stability of mixing uranium within goethite. Increasing uranium content within goethite resulted in increasingly positive formation enthalpies from oxide components. Standard formation enthalpies of $U_{0.5x}Fe_{1-x}OOH$ were as large as 120.1 ± 2.0 kJ/mol relative to their binary oxides, or -441.0 ± 2.4 kJ/mol relative to their constituent elements, at $x = 0.032$. These samples may not have reached equilibrium during hydrothermal treatment, and the role of entropy could not be calculated. The stability of higher uranium content is more representative of mixing energetics between goethite and discrete uranium oxide phases, with structural incorporation being saturated. Lower concentrations contain a higher proportion of total retained uranium. These new results on the thermodynamics of uranium substitution and solid solution formation in goethite under oxic

conditions provide additional perspectives on the pathways by which goethite may inhibit the mobility of aqueous uranium.

3.2 Introduction

Uranium is a toxic radiological contaminant in aqueous environments. Mine tailings and legacy radioactive waste pose contamination risks to local ecology and water sources for human consumption.[1,2] Persistent exposure to this contaminant may induce long-lasting damage to human health.[3,4] Capturing and inhibiting the mobility of radionuclide leachate from waste storage facilities, e.g., the U.S. DOE Hanford site, may mitigate the potential exposure and damage to the environment and humans.[5–9] Environmentally abundant minerals and corrosion products from radioactive waste repositories, such as iron oxides, may play a crucial role in inhibiting uranium from upon eventual leaching into the environment.[10,11]

Goethite (α-FeOOH) nanoparticles, like other iron bearing minerals, are naturally occurring and are effective at adsorbing toxic heavy metal ions under a variety of naturally occurring environmental conditions.[12–16] Existing kinetic and structural studies have explored pathways where uranium may be strongly retained along various sites within α-FeOOH.[17,18] Aqueous uranium may be immobilized by nanoscale iron oxide and oxyhydroxide polymorphs through a combination of coprecipitation within their structures and adsorption to their surfaces.[19–27] Changes in surrounding environment or favorable adsorption of competing species may quickly remobilize surface-bound uranium back into water.[28,29] Meanwhile, uranium trapped within the structure of minerals is more recalcitrant to extraction and remobilization. The coordination environment of the restrained uranium has been studied for a variety of iron oxide and oxyhydroxide polymorphs found in various environmental conditions, including those of radiological waste repositories.[30,31]

Studies have primarily explored uranium immobilization through simultaneous U(VI) reduction and goethite transformation.[23,24] Doornbusch et al. claimed that U(V) or U(VI) may substitute for Fe(III) within goethite, fitting a highly distorted octaheral site.[32] This finding has since been disputed, with Kerisit et al. suggesting that their data instead reflected strongly adsorbed uranyl species.[18] By contrast, their own work calculated uranium to instead occupy undistorted, symmetric octahedral sites regardless of U oxidation state.[18] Later studies by McBriarty et al. found their best fit to consist of primarily U(V) and a small fraction of U(VI).[33] Less thoroughly studied is the behavior of U with goethite under oxic conditions, absent of reduced U or Fe species. Soltis et al. confirmed that growth of goethite by oriented attachment may capture U(VI) that is recalcitrant to remobilization in oxic, acidic media.[34] Most of that retained uranium was concluded to be strongly adsorbed, and only a small fraction of U was incorporated into the goethite structure. It is worth noting that each study used different synthesis and washing methods for their samples, which could have impacted their resulting samples and EXAFS data. Regardless of competing interpretations of local coordination and charge compensation schemes, research has consistently demonstrated that goethite can strongly retain uranium and resist its remobilization into aqueous environments. Energy-minimized simulations have predicted local U coordination within goethite. However, there is not yet any data on the formation energetics of these structures.

This work aims to explore the significance and stability of uranium immobilization by the oxic transformation and oriented growth of goethite. Goethite (α-FeOOH) nanoparticles were synthesized with uranium trapped within their structure and along the interfaces of their nanorod aggregates. The resulting product is approximated as α-$U_{0.5x}Fe_{1-x}OOH$ based on its molar ratio of U/Fe. Local U coordination was examined through extended X-ray absorption fine structure (EXAFS). The overall iron oxyhydroxide structure and uranium partitioning were assessed using

X-ray diffraction (XRD) and transmission electron microscopy (TEM). The thermodynamic costs of uranium loading within the goethite host were obtained through high temperature oxide melt solution calorimetry. These techniques complement each other to validate the coordination and corresponding stability of uranium retained within iron oxides. Determining their formation enthalpies relative to mixtures of iron and uranium oxides may constrain stability of uranium retention over geologic timescales. Results from this research expand understanding the potential effectiveness of iron oxides to naturally, or deliberately, inhibit aqueous radionuclide migration.

3.3 Experimental Methods

3.3.1 Synthesis

Synthesis of uranium-incorporated goethite (α-$U_{0.5x}Fe_{1-x}OOH$) began with mixing $Fe(NO_3)_3 \cdot 9H_2O$ (Sigma-Aldrich, ACS Reagent ≥ 98 %) and $UO_2(NO_3)_2 \cdot 9H_2O$ (JT Baker, 'Baker Analyzed' Reagent) in 18.2 MΩ·cm deionized water. Unlike the Fe(II)-catalyzed reaction commonly used for uranium-incorporated goethite synthesis, all work was performed in open air, and water was not deoxygenated.[26] Starting precursors were in their fully oxidized states, preventing the redox interaction that would have occurred between Fe(II) and U(VI). Uranyl concentrations for the five synthesized samples ranged between 0 and 3.15 mM, while maintaining Fe(III) at 41 mM. 10 N NaOH (Fisher Scientific, Certified ACS) was used to titrate the acidic solution up to pH ≥ 13 while stirring at room temperature. A transition to colloidal ferrihydrite was observed around pH 5.6, at which point the precipitate was expected to favorably adsorb the uranyl species.

Hydrothermal treatment was used to accelerate kinetics of the full transformation from ferrihydrite to goethite, preventing secondary phases (e.g., hematite, α-Fe_2O_3) from otherwise forming.[35] 120 mL of the colloidal suspension was transferred to a 200 mL Teflon-lined hydrothermal vessel from Parr Instrument Co. The vessel was then sealed and placed into an oven at 180 °C for 24 hours, followed by gradual cooling down in air.

The product fully transformed into α-FeOOH and collected at the bottom of the vessel. Aliquots of the supernatant were preserved for elemental concentration analysis, which was used to determine uranyl concentration in solution after synthesis. The precipitate was washed multiple times with DI water while agitating to remove residual salts, followed by centrifugation to collect the nanoparticles. The reaction for producing the final product is reported as **Eqn. 3.1**:

$$0.5x(UO_2)^{2+}{}_{(aq)} + (1-x)Fe^{3+}{}_{(aq)} + OH^-{}_{(aq)} + (1-x)O_{2(g)} \xrightarrow{180°C} U_{0.5x}Fe_{1-x}OOH_{(s)} \tag{3.1}$$

Because no redox is involved, this proposed reaction differs from conventional Fe(II)-catalyzed goethite formation (**Eqn. 3.2**) and corresponding hypothesized U-FeOOH induced by U(VI)/Fe(II) redox interactions (**Eqn. 3.3**).

$$xFe^{2+}{}_{(aq)} + (2-x)Fe^{3+}{}_{(aq)} + (6-x)(OH)^-{}_{(aq)} \xrightarrow{180°C} 2(Fe_{1-x}OOH)_{(s)} + 2H_2O_{(l)} \tag{3.2}$$

$$x(UO_2)^{2+}{}_{(aq)} + xFe^{2+}{}_{(aq)} + (2-x)Fe^{3+}{}_{(aq)} + 6(OH)^-{}_{(aq)} \xrightarrow{180°C} U_x(Fe_{1-x}OOH)_{2(s)} + 2H_2O_{(l)} \tag{3.3}$$

This study focused on the stability of uranium well-immobilized within hematite particles, absent of surface-bound uranyl and colloidal uranium-containing impurities. Additional washing steps using a solution of HCl below pH 3 were performed to achieve this, remobilizing weakly retained uranium back into solution.[28] Subsequent water washes were performed to clean and neutralize the product. The sample was then dispersed in ethanol and dried in air at 80 °C overnight.

3.3.2 Structural and Electronic Characterization

Identification of the desired iron oxide phase, as well as the absence of undesired secondary phases, is imperative for properly analyzing calorimetric data. Powder X-ray diffraction (PXRD) of the final product was performed to validate phase purity and crystallinity (Bruker D8 Advance, Cu K-α_I). Average size of the particles was approximated from crystallite size (d), which was then used to interpolate surface energy contributions from the nanoparticles. Crystallite sizes were compared to literature values to approximate surface energy and account for contributions to calorimetry results. Transmission electron microscopy (TEM) was performed to validate phase purity and crystallite size shown by XRD, as well assess uranium distribution along the iron oxide particles.[36] High-angle annular dark field (HAADF) imaging and brightfield imaging in STEM mode were performed using a JEOL 2100F at 200 kV and FEI Tecnai F30 at 300 kV. Samples were prepared by dispersing and sonicating powders in IPA and dropped onto carbon-backed Cu mesh grids. The grids were then baked out overnight at 80 °C and plasma-cleaned prior to imaging. The local coordination environment of uranium retained within goethite were determined by EXAFS. Uranium L_{III}-edge (17.1663 keV) spectra were collected on beamline B-18, Diamond Light Source (DLS), under liquid nitrogen in fluorescence mode.

3.3.3 Stoichiometry Determination

Thermogravimetric analysis (TGA) was run in parallel with differential scanning calorimetry (DSC) using a Setaram Labsys Evo. Powders were pressed into pellets of 10 – 20 mg and placed in a 100 µL platinum crucible. Samples were heated from 25 °C to ≥ 800 °C at 10 °C/min while flushing the chamber with O_2. TGA quantified the amount of total water adsorbed onto U-goethite particles. Meanwhile, DSC data reported on the heat effects from dehydration and thermal decomposition into hematite. Solid samples were digested in 5 N HCl at 90 °C then diluted to 2 %

HCl for inductively coupled plasma mass spectrometry (ICP-MS) analysis. Molar ratios of each element were then used to calculate the U/Fe stoichiometry of anhydrous product, defined as α-$U_{0.5x}Fe_{1-x}OOH$.

The differences in uranium content between the starting amount, amount remaining in solution after synthesis, and the amount retained in the collected final product, were then used to calculate the amount of uranium lost to the successive washing and acid-leaching procedures. Lost uranium here is considered a combination of uranyl species adsorbed to goethite surfaces, poorly crystalline uranium-containing colloids, and losses from repeated washing and centrifugation steps. At the same time, Fe concentrations confirmed that all the introduced Fe(III) had precipitated by the end of the reaction.

3.3.4 Calorimetry

High temperature oxide melt solution calorimetry was performed using a custom-built twin Calvet calorimeter held at 700 °C with sodium molybdate ($3Na_2O \cdot 4MoO_3$) as the solvent.[37] Approximately ≤ 7mg of sample was pelletized and dropped into the melt for each of multiple measurements. Oxygen gas was flushed above the solvent at 51.6 mL/min and bubbled through it at 5.9 mL/min. Doing so maintained a consistent atmosphere above the molten solvent, while also mechanically mixing and accelerating dissolution of samples. The enthalpy of dissolution (ΔH_{ds}) was calculated by integrating the measured heat flow from dissolving the powder over time. This value was then used to calculate the standard formation enthalpy of the material. Calorimetric measurements were calibrated against bulk α-Al_2O_3 powder, which yield heat effects of comparable magnitude. The thermochemical cycles used to calculate formation enthalpies from elements and from oxides are reported in **Appendix B, Table SI-3**.

3.4 Results and Discussion

3.4.1 Synthesis and Characterization of α-$U_{0.5x}Fe_{1-x}OOH$

We observe the formation of crystalline α-FeOOH to be absent of any uranium oxide or secondary iron oxide phases (**Figure 3.1**).[38] Rietveld refinement of XRD patterns between all reveal an average crystallite size of 21.5 ± 1.7 nm, suggesting that the wide range of uranyl concentrations used during synthesis had minimal impact on the size of individual grains. TEM imaging reveals this crystallite size roughly matches the width of most nanorods. The approximate size and corresponding surface areas of these U-loaded goethite samples fall within the range where surface energy contributions may affect their thermodynamic stability. The surface energies of goethite nanoparticles have been reported to affect their overall standard formation enthalpies. Enthalpic values for a uranium-free reference were interpolated from published values for nano-goethite.[39,40] The resulting ΔH_{ds} and ΔH°_f values were then used as a point of reference for uranium-incorporated samples in this study.

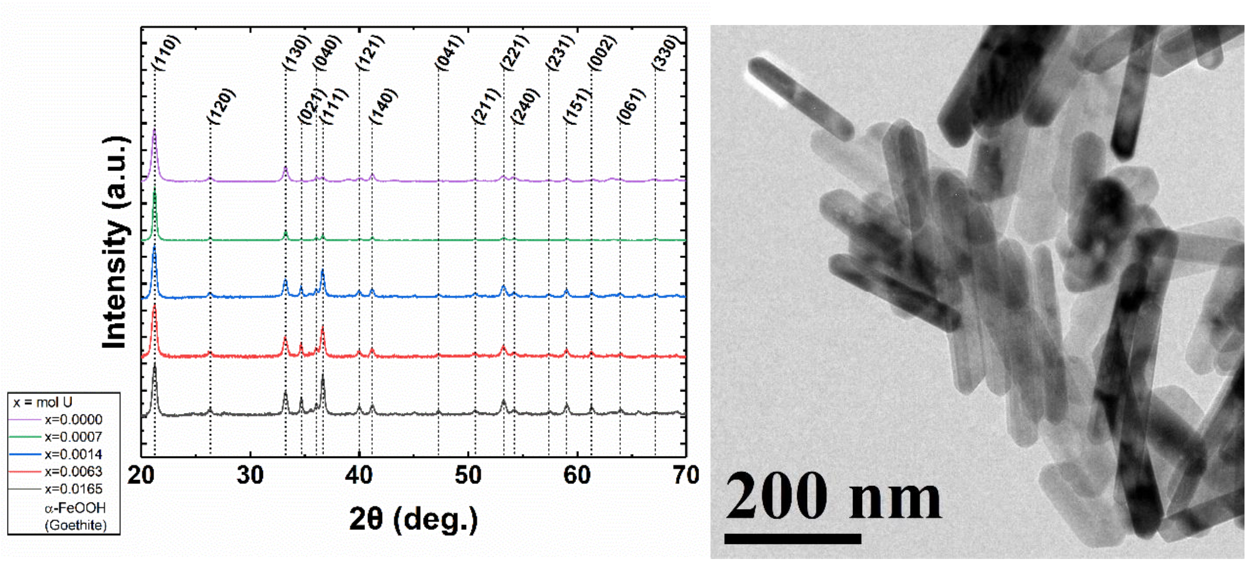

Figure 3.1 XRD patterns of single-phase goethite coprecipitated with varying initial concentrations of uranyl ions (left) and representative bright field TEM micrograph of crystalline goethite nanoparticles (right).

Uranium is visible in HAADF TEM and highlighted by its high atomic number relative to Fe. The centers of the goethite nanorods are too thick to resolve and identify uranium occupation within crystallographic sites. However, U atoms are prevalent along the boundaries of aggregated goethite rods and consistently scattered across the entirety of each nanorod (**Figures 3.2-3.3**). EXAFS results reveal that some retained uranium is structurally incorporated within the goethite structure, rather than along grain boundaries.

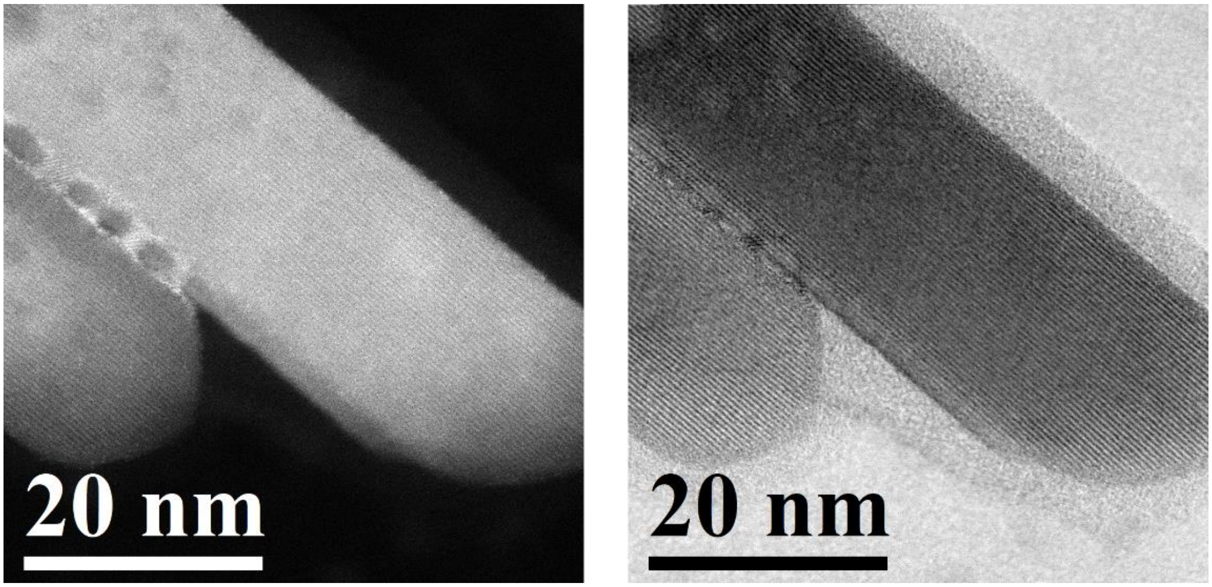

Figure 3.2 Representative HAADF (left) and brightfield (right) TEM micrographs of U (0.62 mol %) in goethite, largely collected along grain boundaries. Bright spots in HAADF result from high atomic mass and are indicative of the presence of uranium.

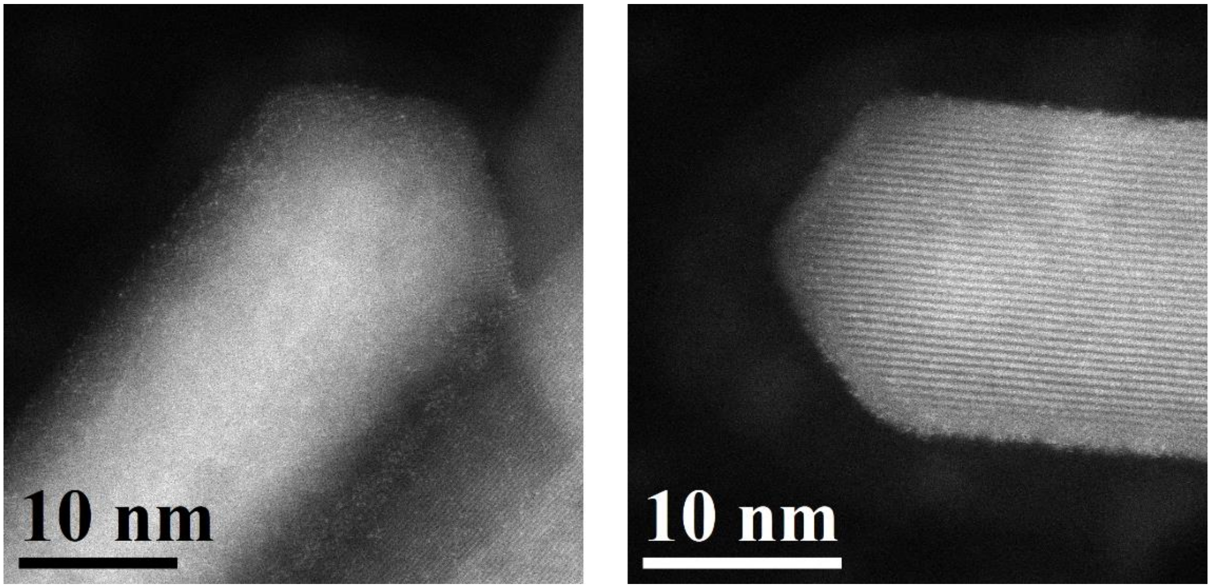

Figure 3.3 HAADF TEM micrographs of goethite nanorods with 0.62 mol % uranium (bright spots result from atomic number contrast) incorporated along lattice fringes.

3.4.2 Uranium Coordination

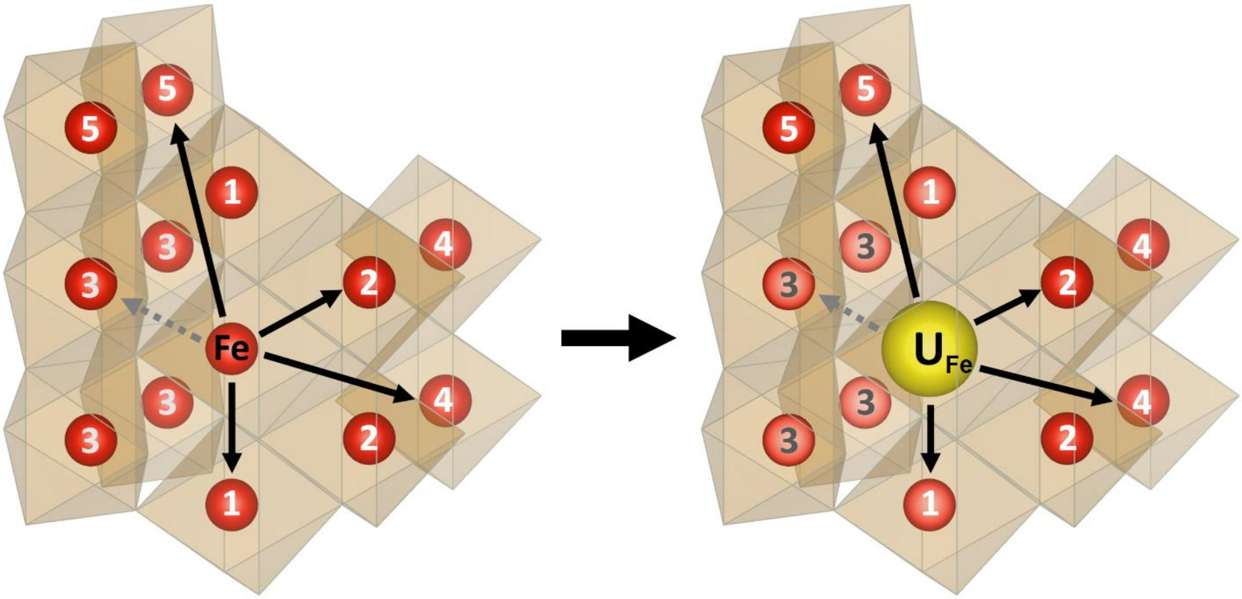

Figure 3.4 Effects of U-Fe substitution on goethite structure, as calculated from U L$_{III}$ EXAFS. Coordination of Fe site #3 decreases from 4-fold to 2-fold after U incorporation. Calculated distances are compared to literature results in **Table 3.1**.

U L$_{III}$-edge spectra of 0.07 mol % U in goethite reveal that the axial oxygen bonds characteristic of uranyl are retained after hydrothermal incorporation into goethite, albeit with decreased coordination and minor elongation (**Table 3.1**). Considering the phase purity of the low U-content sample, we attribute our U-O spectra largely to uranium retained within goethite, rather than any potential hematite or surface uranyl that might otherwise have been present. The H-coordinated oxygens between edge-sharing Fe atoms are consistently present with increased bond lengths relative to those typically bound to surrounding Fe sites. The increase in effective distance from 2.089 Å to 2.225 Å is attributed to the large difference in ionic radius between U(VI) (0.870 Å) and Fe(III) (0.785 Å).[41]

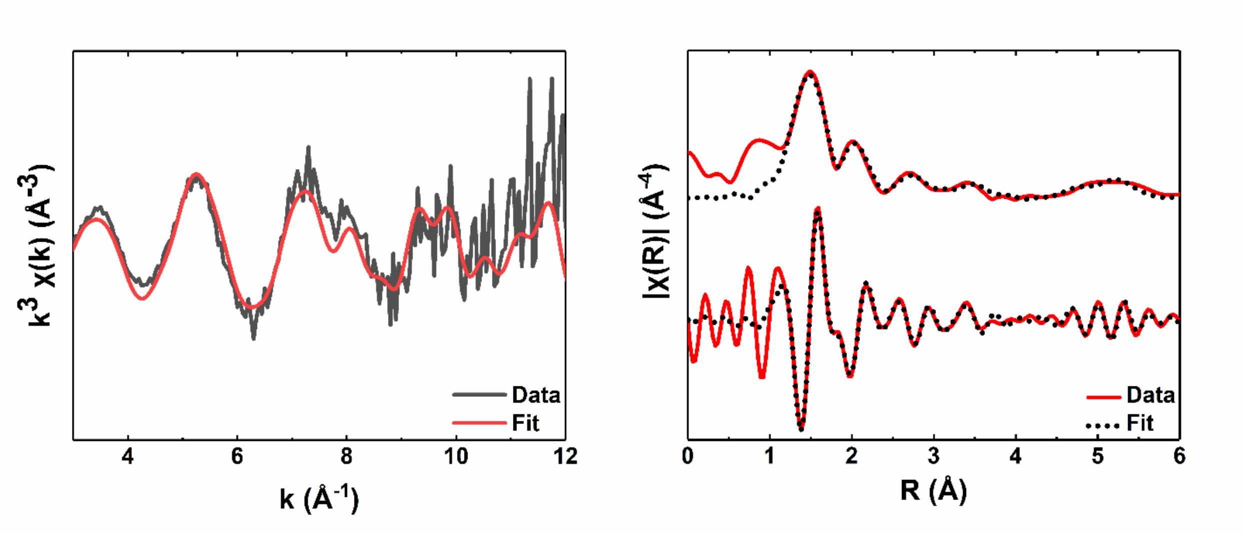

Figure 5 Uranium L_{III}-edge EXAFS spectrum (left) and its Fourier transform (right) from 0.07 mol % U in goethite.

Our results reveal coordination of uranium to multiple neighboring iron sites, which serves as evidence of structural incorporation and occupation of iron sites within the goethite structure (**Figures 3.4-3.5, Table 3.1**). Every resolved U-Fe shell expanded relative to reference goethite bond lengths. U-Fe shells were resolved up to 5.57 Å, most notably with reduced coordination of the corner-sharing Fe shell (3.65Å; R_{eff} 3.43 Å) from four-fold down to two-fold. Increasing coordination number of the corner-sharing shell beyond 2 increased the degree of disorder; our fit concluded that only half of the 4 corner-sharing Fe sites are present around a U-substituted Fe site. Statistical F-tests showed all resolved Fe shells are present with high confidence (**Appendix B, Table SI-1, SI-2**).[42]

Table 3.1 EXAFS fit results demonstrating uranium incorporation (0.07 mol %) to α-FeOOH, using a k-range of 3.0 – 11.8.

Fig. 4	U-path	CN	ΔCN	R_{ref} (Å)	R_{lit} (Å)[32]	**R (Å)**	ΔR (Å)	σ^2 (Å^2)	ΔE_0 (eV)	$S0^2$	χ_v^2	R_{fit}
	O_{Axial}	1.3	-0.7	1.77(8)	1.82	**1.81(9)**	0.04(0)	0.004(3)	8.7 ± 1.0	1.0	3.141	0.010
	O_H	2.0	-1.0	2.08(8)	2.22	**2.22(5)**	0.13(6)	0.004(0)				
	$O_{Equitorial}$	2.7	-2.3	2.43(4)	2.41	**2.41(4)**	-0.02(0)	0.004(0)				
Fe-1	Fe_{Edge1}	1.8	-0.7	3.01(2)	3.25	**3.25(8)**	0.24(5)	0.004(5)				
Fe-2	Fe_{Edge2}	2.0	--	3.29(1)	3.45	**3.45(9)**	0.16(8)	0.004(5)				
Fe-3	Fe_{Corner}	2.0	-2.0	3.43(1)	3.69	**3.65(4)**	0.22(3)	0.005(8)				
Fe-4	$Fe_{C\text{-}C}$	4	--	5.27(7)	--	**5.32(8)**	0.05(1)	0.006(5)				
Fe-5	$Fe_{E\text{-}C\text{-}C}$	8	--	5.47(6)	--	**5.56(9)**	0.09(3)	0.011(5)				
		CN – coordination number R – atomic distance ΔR – difference from reference values σ^2 – Debye-Waller factor ΔE_0 – energy shift from U L_{III} $S0^2$ – amplitude factor χ_v^2 – reduced χ square value R_{fit} – goodness of fit										

Acquired EXAFS data partially agree with existing literature on uranium-incorporated goethite, in that uranium coordinates to neighboring Fe shells. However, our samples were not subjected to reductive processes, and our spectra appear to more closely align with U(VI) than U(V).[27] Our fits most closely resemble those of Doornbusch et al. (**Table 3.1, R_{lit}**).[32] Their findings have been questioned due to the low amplitude reduction factor ($S0^2$) of 0.65 used to fit their data, whereas values of ≥ 0.9 are more typical.[18] Our fit ($S0^2 = 1.0$) found bond lengths to closely match theirs. The two short axial bonds and four equatorial bonds to oxygen are more characteristic of U retained in hematite – despite no hematite being detected in our system.[26] Our findings confirm that structural incorporation can occur even without Fe(II) catalyzed reduction of U(VI). *Ab initio* molecular dynamics (AIMD) simulations by Kerisit et al. explored potential coordination environments, oxidation states, and charge compensation mechanisms of uranium within goethite.[17,18] Their models determined U(V) to substitute into Fe(III) sites by deprotonation of first shell hydroxyls, with minimal octahedral distortion, and with an edge-sharing Fe vacancy. Our EXAFS findings corroborate that Fe site substitution is the dominant and preferred U retention pathway, albeit with an alternative local structure (reduced coordination of corner-sharing Fe sites, rather than ancac edge-sharing Fe vacancy). Dissimilarities between our EXAFS spectra and theirs may be ascribed to the substantial differences in synthesis conditions. Previous studies may have explored coordinations unique to redox conditions, whereas the elevated hydrothermal temperatures and hyperalkaline solution in our study may have been favorable for this alternative U configuration.

Clustering along grain boundary interfaces was also resistant to remobilization under acidic conditions and observed through TEM (**Figure 3.2**). In combination with our HAADF TEM findings and their similarities to findings on oriented aggregation of goethite by Soltis et al., we conclude that our hydrothermal conditions facilitate U substitution within Fe sites, especially along aggregate interfaces. Localized vacancy configurations may have been energetically favorable and facilitated by iron site substitution under our specified hydrothermal conditions. It is not yet clear if the same behavior would be observed at ambient temperatures or under anoxic conditions, such as used in the previously mentioned studies. For structurally incorporated uranium ions we hypothesize local distortion of the surrounding oxygen octahedra, vacancy formation in neighboring iron sites for charge balance, and increased metastability of the combined oxide at room temperature.

3.4.3 Stoichiometry – Dehydration

Water loss was measured by TGA, which accounts for surface hydration as well as structural hydration within goethite itself. Water-corrected enthalpy measurements ($\Delta H_{\text{ds-H2O, 700 °C}}$) are reported in **Table 3.2**. Representative TGA and DSC traces are shown in **Figure 3.6**. During heating, the iron oxyhydroxide (goethite) transforms into iron oxide (hematite) (**Eqn. 3.4**). The final Fe_2O_3 mass and total mass change from each experiment are used to calculate the amount of structural and excess hydration within the synthesized U-goethite samples.

$$FeOOH \cdot nH_2O \rightarrow Fe_2O_3 + \left(\frac{1}{2} + n\right) H_2O \tag{3.4}$$

Routine drying after synthesis removes the bulk of physisorbed water. The first observable mass loss resulting from structural water and excess chemisorbed water occurs above 200 °C. Upon heating to higher temperatures, bare goethite and low U-content goethite experience no appreciable changes in mass. Inflections in heat flow at elevated temperatures are therefore attributed strictly to anealing and structural iron oxide changes (γ-Fe_2O_3, α-Fe_2O_3), which do not involve mass change. Heavily loaded goethite (1.6 mol % U) samples experienced mass gain above 500 °C and shortly thereafter mass loss near 600 °C. This behavior agrees with expected reactions from uranium calcination, where oxidation to UO_3 (O mass gain) first occurs, followed by reduction to U_3O_8 (O mass loss).[43,44] This easily observable behavior corroborates observations from HAADF TEM, where uranium is largely clustered between goethite nanorod interfaces. This partitioning, relative to U-Fe substitution, facilitates oxidation and crystallization of embedded uranium at elevated temperatures.

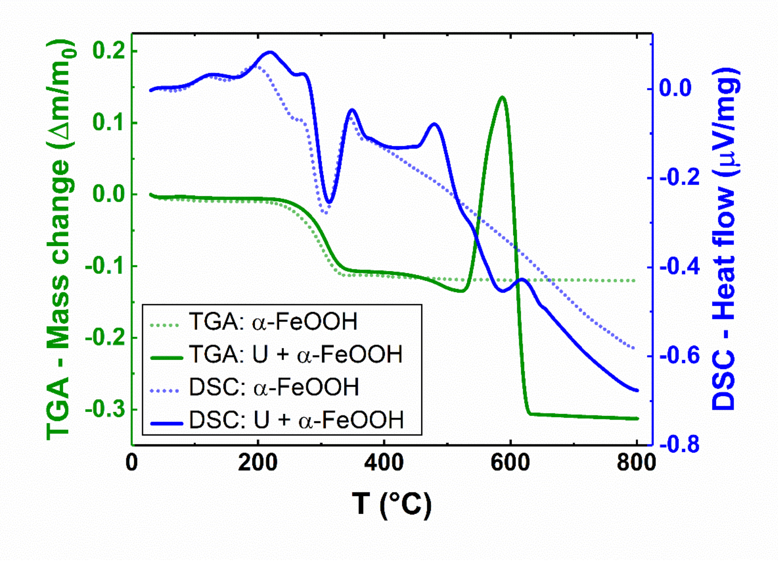

Figure 3.6 Concurrent TGA and DSC traces of $(U_{0.016}Fe_{0.967}OOH)\cdot1.35H_2O$ synthesized using oxic hydrothermal treatment. Differences were too small to resolve between uranium-free and lower uranium content samples.

3.4.4 Stoichiometry – Uranium Remobilization and Retention Pathways

Uranium concentrations within goethite samples were calculated from ICP-MS of acid-digested solids (**Table 3.2**). Mass balance calculations were used with ICP-MS data to determine the amount of uranium that had been weakly adsorbed to precipitate surfaces, coprecipitated into acid-unstable (< pH 3) solids, and strongly incorporated within goethite particles (final product). An upper limit of approximately 1.6 mol % U was found for the studied concentration, temperature, and reaction times. Supernatant concentrations of U and Fe after goethite formation were negligible, indicating complete immobilization of U after α-FeOOH crystallization. The theoretical maximum loading capacity tested (3.15 mM U(VI), 41 mM Fe(III)) was roughly 211 mg U per gram of FeOOH synthesized. As low as 1.66 mg U/g α-FeOOH and as high as 9.47 mg U/g α-FeOOH were calculated to be strongly retained within goethite Fe sites and grain boundaries. Saturation of uranium within goethite was not observed when increasing initial uranyl concentration, suggesting maximum incorporation concentration to be somewhere higher than levels explored in this study. The relative favorability of each retention pathway is shown in **Figure 3.7**. All aqueous uranium was immobilized following each tested synthesis condition, and the most favorable route at studied uranyl concentrations was invariably adsorption. This behavior contrasts against our current work with hematite, where lattice and grain boundary incorporation comprise most of the captured uranium at lower U(VI)/Fe(III) ratios.

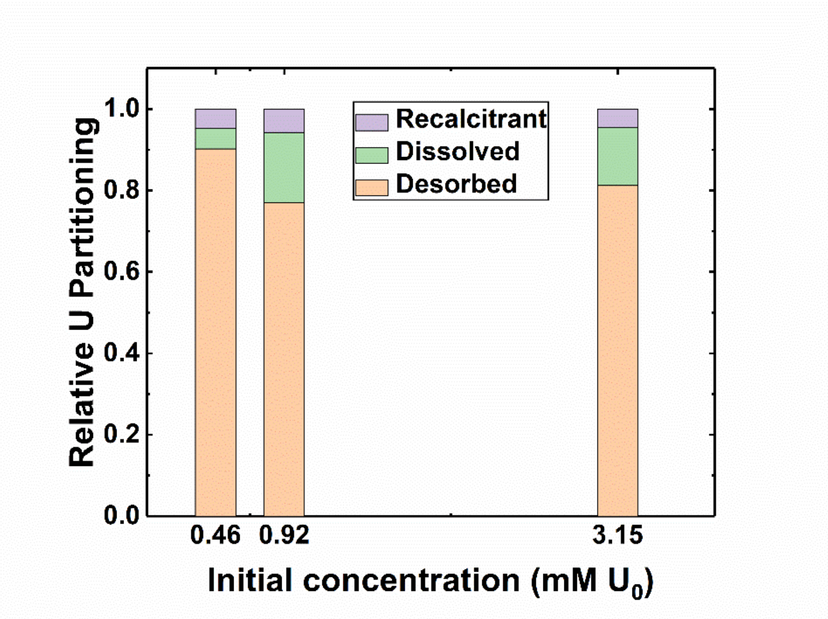

Figure 3.7 Effect of U_0 on uranium partitioning to immobilization pathways, based on ICP-MS and mass balance calculations. Results are shown as fractions of total uranium in the system.

Uranium immobilization pathways under hydrothermal conditions may vary depending on initial uranyl concentrations and on redox conditions. The kinetics of uranium immobilization could be elucidated in the future by exploring longer time periods and a wider range of hydrothermal conditions. The lack of redox cycling between U(VI) and Fe(II) during aerobic goethite crystallization may hinder the ability to capture and retain aqueous uranium within its structure. Repeating these studies on well characterized U-FeOOH may reveal the significance of redox chemistry on the extent of uranium incorporation and its resulting thermodynamic stability.

3.4.5 Energetics of Uranium Immobilization

To determine the formation enthalpies of the oxides themselves, hydration contributions needed to be removed. As determined by TGA, each sample retained quantified amounts of stoichiometric and adsorbed water. The bulk water contributions at 700 °C were approximated as 69.0 kJ/mol H_2O, which is the enthalpy of heating liquid water at ambient temperature to form water vapor (which is released) at calorimeter temperature. and subtracted from measured values to obtain the enthalpy of drop solution of the anhydrous material.[45] An additional -19.4 kJ/mol contribution from chemically bound water (which constitutes 59% of total adsorbed water at a relative humidity of 43 – 53%) was also corrected for.[39,40] Water corrected measurements were reported as $\mathbf{\Delta H_{ds\text{-}H_2O}}$ and used for subsequent thermodynamic calculations. **Table 3.2** provides a summary of uranium concentrations and corresponding thermodynamic values.

Decreased stability from high surface areas contributed to measured calorimetric values of nanoparticles. Nanophase α-FeOOH with a representative surface area of 11.1 x 10^3 m^2/mol has been reported to have a surface energy of 0.60 ± 0.10 J/m^2.[39] This uranium-free goethite of comparable geometry and corresponding surface energy serves as the reference point for our measured calorimetric values. Differences in surface energetics of studied nanoparticles are negated from enthalpy calculations, and nanocrystal surface energy contributions may be separately calculated as needed per specific modeling case.

Table 3.4 Measured and calculated thermodynamic properties for $U_{0.5x}Fe_{1-x}OOH \cdot nH_2O$. Formation enthalpy calculations are described in **Appendix B, Table SI-3**.

0.5x (mmol U)	n (mol H_2O)	$\Delta H_{ds,\ 700°C}$ (kJ/mol)	$\Delta H_{ds\text{-}H_2O,\ 700°C}$ (kJ/mol)	$\Delta H°_{f,el}$ (kJ/mol)	$\Delta H°_{f,ox}$ *vs* α-Fe_2O_3 & γ-UO_3 (kJ/mol)	$\Delta H°_{f,ox}$ *vs* α-FeOOH & γ-UO_3 (kJ/mol)
0.00	0.28	100.6 ± 1.51	81.63 ± 1.51	-555.31 ± 2.68	0.69 ± 2.21	3.06 ± 2.33
0.72	0.10	85.35 ± 1.06	76.92 ± 1.06	-550.78 ± 2.47	5.36 ± 1.94	7.70 ± 2.08
1.36	0.71	100.72 ± 1.08	43.59 ± 1.08	-517.61 ± 2.47	38.66 ± 1.94	40.98 ± 2.08
6.25	0.07	62.69 ± 0.96	57.22 ± 0.96	-532.42 ± 2.42	24.82 ± 1.88	26.95 ± 2.02
16.49	1.35	56.33 ± 0.86	-52.16 ± 0.88	-425.51 ± 2.39	133.77 ± 1.84	135.52 ± 1.98

n – excess water bound by chemisorption and physisorption
$\Delta H_{ds,\ 700°C}$ – enthalpy of drop solution
$\Delta H_{ds\text{-}H_2O,\ 700°C}$ – water-corrected enthalpy of drop solution
$\Delta H°_{f,el}$ – standard formation enthalpy relative to constituent elements
$\Delta H°_{f,ox}$ – standard formation enthalpy relative to binary constituents

With increasing uranium concentration, the energetic stability of the composite oxide decreases relative those of its constituent elements (**Table 3.2, $\Delta H°_{f,el}$**) and its binary oxide constituents (**Table 3.2, $\Delta H°_{f,ox}$**). Formation enthalpies with any amount of uranium indicate metastability relative to separate binary oxides (α-Fe_2O_3 or α-FeOOH and UO_x). Enthalpic trends for the collective retained uranium are shown as functions of initial uranyl concentrations in **Figure 3.8**. Formation enthalpy trends relative to binary uranium oxides of lower oxidation states are nearly identical and provided in **Appendix B, Figure SI-1**. Relative to binary oxides, structural incorporation progressively increases (makes less exothermic) the formation enthalpy of the mixed oxide. Incorporation at these loading concentrations is metastable under standard conditions and may be aided by entropic contributions, or it may represent metastability dependent on kinetics of incorporation. It is unclear whether entropy played a significant role in compensating for the positive formation enthalpies. There was no evidence of the hydrothermal conditions reaching equilibrium, and entropy could not be calculated.

In contrast to conventional aging studies, hydrothermal treatment typically allows nanoparticles to fully crystallize, aggregate, grow, and ultimately stabilize while annealing defects.[46,47] If contaminated with aqueous uranyl species under such conditions, adsorbed uranium atoms are provided the opportunity to favorably diffuse into the iron oxide lattice. Thermodynamic stability of the mixed phase at elevated temperatures allows this process to occur. We therefore hypothesize that accelerated diffusion kinetics and expansion of the host lattice under elevated synthesis temperatures enables favorable uranium migration into Fe sites.

Uranium may be well retained through two routes within goethite nanoparticles. As evidenced by TEM, uranium atoms may cluster along the boundaries of goethite aggregates and along goethite lattice fringes (**Figures 3.2-3.3)**. In addition, EXAFS interpretations confirm uranium can occupy iron sites throughout the host structure. However, quantitative distinctions in stability arising from lattice incorporation versus grain boundary confinement cannot be made.

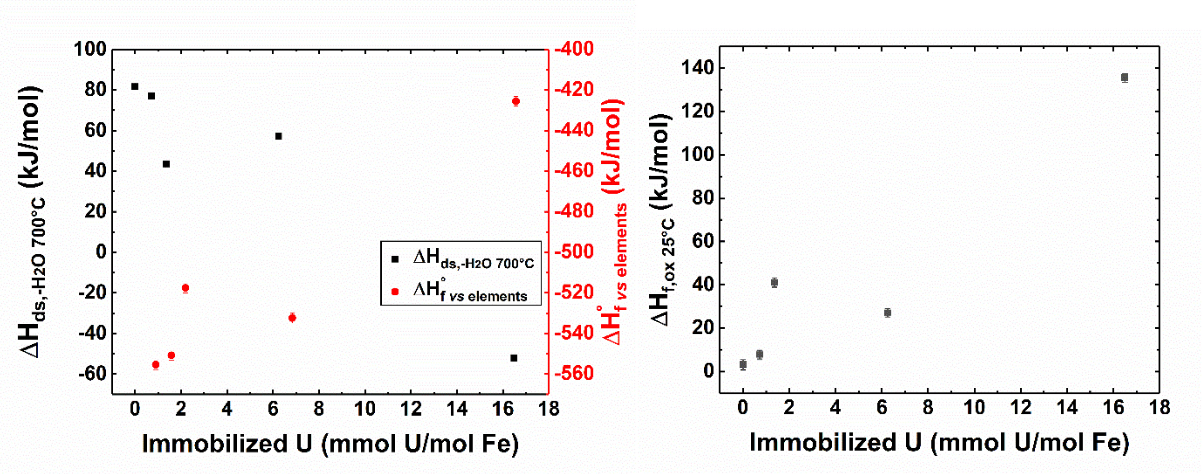

Figure 3.8 Water corrected heat of dissolution in $3Na_2O{\cdot}4MoO_3$ at 700 °C and calculated standard formation enthalpy in relation to constituent elements (U, F, O) (left). Standard formation enthalpy in relation to binary oxides (γ-UO_3, α-Fe_2O_3) (right).

Thermodynamic results reveal an interplay between maximizing uranium concentration within goethite (as an effective and efficient remediation medium) and maximizing energetic stability of the contained uranium. Reported formation enthalpies represent the stability of goethite with strongly bound uranium within its structure. Our findings reveal increasing energy costs and decreased stability with increasing levels of uranium incorporation under highly alkaline (pH ≥ 13), aerobic environments. Anoxic, Fe(II)-catalyzed goethite, which have notable differences in local U-Fe coordination, may also have an appreciable difference in thermodynamic stability that is worth further study.

Results from this project provide data for understanding the fate of uranium over extended timescales, where gradual exposure to highly alkaline geological environments may induce the transport of uranium into the environment. Lattice incorporation and grain boundary confinement, under elevated temperatures and aerobic environments, are achievable and metastable under ambient conditions. Expanding this thermodynamic study to goethite formed under anoxic conditions may reveal contrasting thermodynamic behavior. The Fe(II)-induced transformation of goethite and uranium incorporation from Fe(II)/U(VI) redox interactions may be representative of oxygen-deficient radioactive waste repositories. Further thermodynamic studies of uranium-iron oxide interactions are necessary to better understand the potential impact of environmentally abundant iron-bearing minerals under varying natural and engineered environments.

3.5 Acknowledgements

This work was supported by the U.S. Department of Energy, Office of Basic Energy Sciences, grant DE-FG02-97ER14749 (Thermodynamics of Minerals Stable near Earth's Surface). Support was also provided by the Nuclear Regulatory Commission through the Advancing Scientific Careers to Enhance Nuclear Technologies (ASCENT) program. We also acknowledge the University of Manchester Department of Earth and Environmental Sciences and Diamond Light Source B18 Beamline for funding and facilitating EXAFS studies.

3.6 References

1. Chen, A., Shang, C., Shao, J., Zhang, J. & Huang, H. The application of iron-based technologies in uranium remediation: A review. *Sci. Total Environ.* **575**, 1291–1306 (2017).
2. Bots, P. *et al.* Formation of stable uranium(VI) colloidal nanoparticles in conditions relevant to radioactive waste disposal. *Langmuir* **30**, 14396–14405 (2014).
3. Kurttio, P. *et al.* Renal effects of uranium in drinking water. *Environ. Health Perspect.* **110**, 337–342 (2002).
4. Orloff, K. G. *et al.* Human exposure to uranium in groundwater. *Environ. Res.* **94**, 319–326 (2004).
5. Ojovan, M. I., Pankov, A. & Lee, W. E. The ion exchange phase in corrosion of nuclear waste glasses. *J. Nucl. Mater.* **358**, 57–68 (2006).
6. Neeway, J. J. *et al.* Ion-exchange interdiffusion model with potential application to long-term nuclear waste glass performance. *J. Phys. Chem. C* **120**, 9374–9384 (2016).
7. Peterson, R. A. *et al.* Review of the Scientific Understanding of Radioactive Waste at the U.S. DOE Hanford Site. *Environ. Sci. Technol.* **52**, 381–396 (2018).
8. Goel, A., McCloy, J. S., Pokorny, R. & Kruger, A. A. Challenges with vitrification of Hanford High-Level Waste (HLW) to borosilicate glass – An overview. *J. Non-Crystalline Solids X* **4**, 100033 (2019).
9. *Final Review of the Study on Supplemental Treatment Approaches of Low-Activity Waste at the Hanford Nuclear Reservation*. *Final Review of the Study on Supplemental Treatment Approaches of Low-Activity Waste at the Hanford Nuclear Reservation* (2020). doi:10.17226/25710
10. Dodge, C. J. *et al.* Association of uranium with iron oxides typically formed on corroding steel surfaces. *Environ. Sci. Technol.* **36**, 3504–3511 (2002).
11. Schäfer, T. & Denecke, M. A. Nuclear waste repository research at the micro- to nanoscale. *AIP Conf. Proc.* **1221**, 181–187 (2010).
12. Villalobos, M., Trotz, M. A. & Leckie, J. O. Surface complexation modeling of carbonate effects on the adsorption of Cr(VI), Pb(II), and U(VI) on goethite. *Environ. Sci. Technol.* **35**, 3849–3856 (2001).
13. Phuengprasop, T., Sittiwong, J. & Unob, F. Removal of heavy metal ions by iron oxide coated sewage sludge. *J. Hazard. Mater.* **186**, 502–507 (2011).
14. Frierdich, A. J. *et al.* Inhibition of trace element release during Fe(II)-activated recrystallization of Al-, Cr-, and Sn-substituted goethite and hematite. *Environ. Sci. Technol.* **46**, 10031–10039 (2012).

15. Guo, H. & Barnard, A. S. Naturally occurring iron oxide nanoparticles: Morphology, surface chemistry and environmental stability. *J. Mater. Chem. A* **1**, 27–42 (2013).

16. Zhang, X. *et al.* Mn-substituted goethite for uranium immobilization: A study of adsorption behavior and mechanisms. *Environ. Pollut.* **262**, (2020).

17. Kerisit, S., Felmy, A. R. & Ilton, E. S. Atomistic simulations of uranium incorporation into iron (hydr)oxides. *Environ. Sci. Technol.* **45**, 2770–2776 (2011).

18. Kerisit, S., Bylaska, E. J., Massey, M. S., McBriarty, M. E. & Ilton, E. S. Ab initio molecular dynamics of uranium incorporated in goethite (α-FeOOH): Interpretation of X-ray absorption spectroscopy of trace polyvalent metals. *Inorg. Chem.* **55**, 11736–11746 (2016).

19. Waite, T. D., Davis, J. A., Payne, T. E., Waychunas, G. A. & Xu, N. Uranium(VI) adsorption to ferrihydrite: Application of a surface complexation model. *Geochim. Cosmochim. Acta* **58**, 5465–5478 (1994).

20. Sherman, D. M., Peacock, C. L. & Hubbard, C. G. Surface complexation of U(VI) on goethite (α-FeOOH). *Geochim. Cosmochim. Acta* **72**, 298–310 (2008).

21. Nico, P. S., Stewart, B. D. & Fendorf, S. Incorporation of oxidized uranium into Fe (Hydr)oxides during Fe(II) catalyzed remineralization. *Environ. Sci. Technol.* **43**, 7391–7396 (2009).

22. Stewart, B. D., Nico, P. S. & Fendorf, S. Stability of uranium incorporated into Fe (hydr)oxides under fluctuating redox conditions. *Environ. Sci. Technol.* **43**, 4922–4927 (2009).

23. Boland, D. D., Collins, R. N., Payne, T. E. & Waite, T. D. Effect of amorphous Fe(III) oxide transformation on the Fe(II)-mediated reduction of U(VI). *Environ. Sci. Technol.* **45**, 1327–1333 (2011).

24. Boland, D. D., Collins, R. N., Glover, C. J., Payne, T. E. & Waite, T. D. Reduction of U(VI) by Fe(II) during the Fe(II)-accelerated transformation of ferrihydrite. *Environ. Sci. Technol.* **48**, 9086–9093 (2014).

25. Massey, M. S., Lezama-Pacheco, J. S., Michel, F. M. & Fendorf, S. Uranium incorporation into aluminum-substituted ferrihydrite during iron(II)-induced transformation. *Environ. Sci. Process. Impacts* **16**, 2137–2144 (2014).

26. Massey, M. S. *et al.* Competing retention pathways of uranium upon reaction with Fe(II). *Geochim. Cosmochim. Acta* **142**, 166–185 (2014).

27. McBriarty, M. E. *et al.* Trace Uranium Partitioning in a Multiphase Nano-FeOOH System. *Environ. Sci. Technol.* **51**, 4970–4977 (2017).

28. Burns, W. G., Hughes, A. E., Marples, J. A. C., Nelson, R. S. & Stoneham, A. M. Effects of radiation on the leach rates of vitrified radioactive waste. *J. Nucl. Mater.* **107**, 245–270 (1982).

29. Smith, K. S. Metal Sorption on Mineral Surfaces. in *The Environmental Geochemistry of Mineral Deposits* 161–182 (Society of Economic Geologists, 1997). doi:10.5382/Rev.06.07

30. Duff, M. C., Coughlin, J. U. & Hunter, D. B. Uranium co-precipitation with iron oxide minerals. *Geochim. Cosmochim. Acta* **66**, 3533–3547 (2002).

31. Ohnuki, T. *et al.* Change in Sorption Characteristics of Uranium during Crystallization of Amorphous Iron Minerals. *J. Nucl. Sci. Technol.* **34**, 1153–1158 (1997).

32. Doornbusch, B., Bunney, K., Gan, B. K., Jones, F. & Gräfe, M. Iron oxide formation from FeCl2 solutions in the presence of uranyl (UO_2^{2+}) cations and carbonate rich media. *Geochim. Cosmochim. Acta* **158**, 22–47 (2015).

33. McBriarty, M. E. *et al.* Trace Uranium Partitioning in a Multiphase Nano-FeOOH System. *Environ. Sci. Technol.* **51**, 4970–4977 (2017).

34. Soltis, J. A. *et al.* Can mineral growth by oriented attachment lead to incorporation of uranium(vi) into the structure of goethite? *Environ. Sci. Nano* **6**, 3000–3009 (2019).

35. Cornell, R. M. & Schwertmann, U. The Iron Oxides. in *Iron Oxides in the Laboratary* **164**, 5–18 (Wiley-VCH Verlag GmbH, 2003).

36. Ilton, E. S. *et al.* Reduction of U(VI) incorporated in the structure of hematite. *Environ. Sci. Technol.* **46**, 9428–9436 (2012).

37. Navrotsky, A. Progress and New Directions in Calorimetry: A 2014 Perspective. *J. Am. Ceram. Soc.* **97**, 3349–3359 (2014).

38. Hexiong, Y., Ren, L., Downs, R. T. & Costin, G. Goethite, α-FeO(OH), from single-crystal data. *Acta Crystallogr. Sect. E Struct. Reports Online* **62**, (2006).

39. Mazeina, L. & Navrotsky, A. Surface enthalpy of goethite. *Clays Clay Miner.* **53**, 113–122 (2005).

40. Mazeina, L. & Navrotsky, A. Enthalpy of water adsorption and surface enthalpy of goethite (α-FeOOH) and hematite (α-Fe2O3). *Chem. Mater.* **19**, 825–833 (2007).

41. Shannon, R. D. Revised effective ionic radii and systematic studies of interatomic distances in halides and chalcogenides. *Acta Crystallogr. Sect. A* **32**, 751–767 (1976).

42. Downward, L., Booth, C. H., Lukens, W. W. & Bridges, F. A variation of the F-test for determining statistical relevance of particular parameters in EXAFS fits. in *AIP Conference Proceedings* (2007). doi:10.1063/1.2644450

43. Guo, X. *et al.* Thermodynamics of formation of coffinite, $USiO_4$. *Proc. Natl. Acad. Sci.* **112**, 6551–6555 (2015).

44. Guo, X., Wu, D., Xu, H., Burns, P. C. & Navrotsky, A. Thermodynamic studies of studtite thermal decomposition pathways via amorphous intermediates UO_3, U_2O_7, and UO_4. *J. Nucl. Mater.* **478**, 158–163 (2016).

45. Chase, M. W. NIST-JANAF Thermochemical Tables, 4th Ed. J. Phys. Chem. Ref. Data. 1998, Monograph 9 (Part I and Part II). *Journal of Physical and Chemical Reference Data* **Monograph**, Part I & II (1998).

46. Lam, U. T., Mammucari, R., Suzuki, K. & Foster, N. R. Processing of iron oxide nanoparticles by supercritical fluids. *Ind. Eng. Chem. Res.* **47**, 599–614 (2008).

47. Notini, L. *et al.* The Role of Defects in Fe(II)-Goethite Electron Transfer. *Environ. Sci. Technol.* **52**, 2751–2759 (2018).

Chapter 4

Calorimetric Report on Ferrihydrites

4.1 Intoduction

Ferrihydrite samples were provided by Sean Zigah and Nadine Kabengi at Georgia State University. Formation enthalpies of the ferrihydrites were studied as functions of aging time and water content. At the time of measurements, the samples had aged from 7 months to 23 months.

Enthalpies of formation from binary oxides, α-Fe_2O_3 and H_2O range from 13.4 to 23.9 kJ/mol, indicating energetic metastability. Longer aging times decrease both water content and enthalpy of formation from oxides, making the latter less endothermic (smaller metastability consistent with higher crystallinity). Ferrihydrite samples aged between 13 and 18 months revealed the greatest difference in these parameters, suggesting a kinetically-driven transformation within that time period.

Heats of formation from elements ranged from -668.7 to -784.5 kJ/mol, demonstrating a linear decrease with respect to increasing hydration.. The more positive value (lesser stability) corresponds to highest aging time and lowest water content, while the less positive (higher stability) corresponds to least aging time and highest water content. The greatest shift in stability is still visible between the 13 and 18-month old samples. Enthalpies of formation from elements scale with water content simply because of the contribution of the heat of formation of H_2O from H_2 and O_2. Thus these differences are overwhelmingly due to contributions from water content and do not provide meaningful insight on differences in structural stability. The data are consistent with earlier work by Majzlan et al.[1]

4.2 Experimental Methods

Each sample arrived suspended in water. Each container was sonicated for roughly 1 hour. They were subsequently transferred to petri dishes and left to air dry in a fume hood. The powders were crushed using a mortar and pestle before storage.

The provided samples had been precipitated and aged in water for varying periods of time, from roughly half a year up to two years. These ferrihydrites are compared with samples previously studied by Majzlan et al. Samples studied by Majzlan et al. revealed similar water contents, but the difference in synthesis methods may have significantly impacted their thermodynamic stabilities. Rather than aged for extended periods of time, each ferrihydrite in the prior study was precipitated by constant titration from 0 – 24 hours. Differences in their water content are likely to be attributed to aggregation and water trapping forced by changes in pH. Without time to age, the aggregated particles lacked the time to crystallize and stabilize.

Water content of each sample was determined by measuring change in mass before and after calcining. Approximately 15mg of each sample was heated from 25 °C to 800 °C at a rate of 10 C°/min. The mass change is attributed to water ejected from the samples. Excess water content (**Table 4.1**) is determined according to the following reaction (**Eqn. 4.1**):

$$FeOOH \cdot nH_2O = \frac{1}{2}Fe_2O_3 + \left(\frac{1}{2} + n\right)H_2O \qquad \textbf{(4.1)}$$

To validate the absence of carbonate complexation, ATR-FTIR on the dried samples was performed using a Bruker VERTEX 70 FTIR spectrometer (**Figure 4.1**). No C-O stretching peaks (1465 and 1345 cm^{-1}) were observed, suggesting the absence of carbonate speciation at the ferrihydrite surfaces – therefore the absence of heat effect contributions by carbonates.

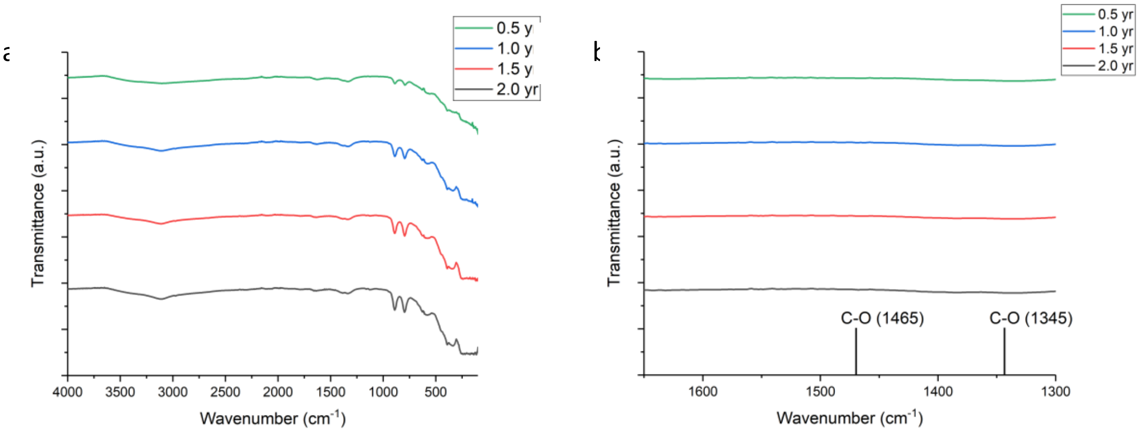

Figure 4.7 ATR-FTIR of ferrihydrite samples (a: whole scan, b: zoomed in to highlight C-O band positions). Evidence of carbonates was not observed.

High temperature oxide melt solution calorimetry was performed at 700 °C with sodium molybdate ($3Na_2O{\cdot}4MoO_3$) as the solvent. Approximately 3 – 5 mg of sample was pelletized and dropped into the calorimetry from ambient temperature into calorimetric conditions. Oxygen gas was flushed above the solvent at 51.6 mL/min and bubbled through it at 5.9 mL/min. This was done to maintain a consistent atmosphere above the molten solvent, as well as mechanically mix and accelerate dissolution of samples. Heat effects were observed as single endothermic peaks that returned to baseline signal within 36 minutes. A minimum of 8 consistent measurements was performed for each sample. The integrated heat effects provided the heat of drop solution, which were used to calculate the formation enthalpies (**Table 4.1)** of each ferrihydrite sample. The thermochemical cycles used to calculate formation enthalpies from elements and from oxides are reported in **Table 2.2**. Tables of individual calorimetric measurements are appended at the end of this report.

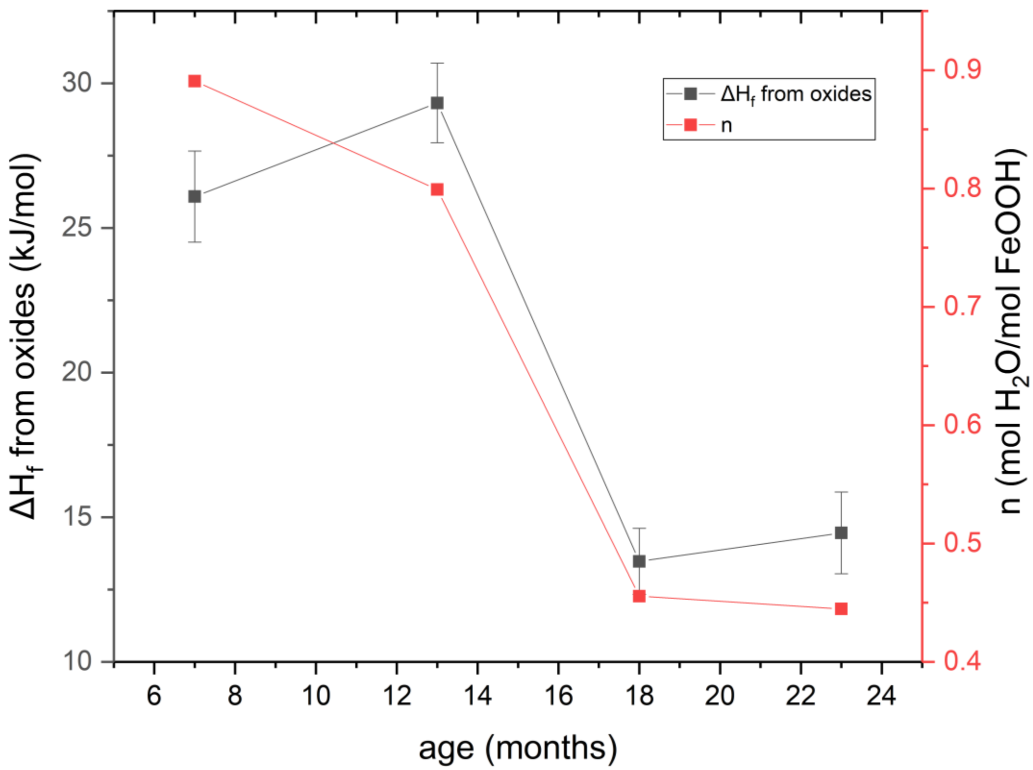

Figure 2.8 Enthalpies of formation from binary oxides and excess water content of ferrihydrites as a function of aging.

4.3 Results and Discussion

A nonlinear trend is observed when comparing formation enthalpies (both from elements and from oxides) as a function of aging (**Figure 4.2**). Although there are clear overall changes in enthalpy with increased aging, the difference between the 13 and 18 months is most pronounced. The change in water content is also most prominent at this stage. This point of greatest change may be explained by exploring structural differences between these intermediate samples.

Table 4.1 Enthalpies of drop solution (**ΔH_{ds}**) and formation (**$\Delta H^{\circ}_{f: \text{elements and oxides}}$**) of ferrihydrites from this study (GSU). Data is also provided for ferrihydrite by Snow and goethite by Mazeina.[2,3] Thermodynamic ferrihydrite values by Majzlan were collected using acid solution calorimetry.[1]

Sample	**Age (mo.)**	**Formula**	**$\Delta H_{ds,NaMo700°C}$ (kJ/mol)**	**$\Delta H_{ds,NaMo700°C}$ (J/g)**	**$\Delta H^{o}_{f,\ elements}$ (kJ/mol)**	***$\Delta H^{o}_{f,\ oxides}$ (kJ/mol)***	***log K****
GSU 6L-Fh1	23	$FeOOH \cdot 0.445H_2O$	98.55 ± 1.32	1017.38 ± 13.61	-668.67 ± 1.92	14.46 ± 1.41	*-2.53*
GSU 6L-Fh2	18	$FeOOH \cdot 0.456H_2O$	100.28 ± 1.02	1033.14 ± 10.55	-672.73 ± 1.73	13.48 ± 1.14	*-2.36*
GSU 6L-Fh3	13	$FeOOH \cdot 0.799H_2O$	108.13 ± 1.29	1047.31 ± 12.46	-755.07 ± 1.90	29.32 ± 1.38	*-5.14*
GSU 6L-Fh4	7	$FeOOH \cdot 0.891H_2O$	117.69 ± 1.49	1121.95 ± 14.23	-784.49 ± 2.04	26.09 ± 1.57	*-4.57*
			$\Delta H_{sol,\ HCl\ 25°C}$ (kJ/mol)	**$\Delta H_{sol,\ HCl\ 25°C}$ (J/g)**			
Majzlan 2L-fh24	--	$FeOOH \cdot 0.520H_2O$	-51.70 ± 0.34	-526.31 ± 3.44	-693.2 ± 1.2	11.4 ± 1.8	*-2.59*
Majzlan 2L-fh12	--	$FeOOH \cdot 0.576H_2O$	-52.90 ± 0.32	-533.10 ± 3.27	-708.1 ± 1.2	12.5 ± 1.8	*-2.00*
Majzlan 2L-fh6	--	$FeOOH \cdot 0.593H_2O$	-52.94 ± 0.42	-531.85 ± 4.25	-712.9 ± 1.2	12.6 ± 1.8	*-2.19*
Majzlan 2L-fh2	--	$FeOOH \cdot 0.801H_2O$	-53.04 ± 0.86	-513.56 ± 8.31	-772.1 ± 1.4	12.8 ± 1.9	*-2.21*
Majzlan 2L-fh0	--	$FeOOH \cdot 0.395H_2O$	-54.88 ± 0.45	-571.90 ± 4.68	-654.1 ± 1.2	14.8 ± 1.8	*-2.25*
Snow 2L-fh	--	$FeOOH \cdot 0.027H_2O$	-49.12 ± 0.36	-549.84 ± 4.01	-542.28 ± 0.76	21.44 ± 0.39	*-3.76*
<u>Goethite</u>			**$\Delta H_{ds,NaMo700°C}$ (kJ/mol)**	**$\Delta H_{ds,NaMo700°C}$ (J/g)**			
Mazeina bulk	--	$\alpha\text{-}FeOOH \cdot 0.08H_2O$	90.2 ± 0.9	999.8 ± 10.0	-560.1 ± 1.4	-4.1 ± 1.9	*0.71*
Mazeina 30nm	--	$\alpha\text{-}FeOOH \cdot 0.15H_2O$	93.7 ± 0.2	1024.3 ± 2.2	-558.5 ± 1.0	-2.5 ± 1.6	*0.44*
Mazeina 9nm	--	$\alpha\text{-}FeOOH \cdot 0.40H_2O$	107.5 ± 1.5	1119.1 ± 15.6	-554.8 ± 2.2	1.2 ± 2.6	*-0.21*
Mazeina 7nm	--	$\alpha\text{-}FeOOH \cdot 0.42H_2O$	109.9 ± 1.2	1139.2 ± 12.4	-555.6 ± 1.6	0.4 ± 2.1	*-0.07*
Mazeina 5nm	--	$\alpha\text{-}FeOOH \cdot 0.80H_2O$	130.0 ± 0.3	1258.9 ± 2.9	-549.7 ± 2.3	6.3 ± 2.6	*-1.10*
Mazeina 2nm	--	$\alpha\text{-}FeOOH \cdot 0.82H_2O$	127.5 ± 1.3	1230.8 ± 12.5	-546.0 ± 1.6	10.0 ± 2.1	*-1.75*

**Approximations from formation relative to α-Fe_2O_3 and H_2O, assuming negligible entropy contribution.*

The increasing stability, as defined as formation enthalpy from hematite and water, as a function of aging period is expected. It is known that ferrihydrites are metastable relative to hematite and may slowly transform into hematite over time. Present results are hypothesized to be due to a combination of crystallization and coarsening of ferrihydrite particles. Such behavior would decrease surface energy and water binding sites and provide better crystallinity. It is interesting to note that the more aged ferrihydrites converge towards values from Majzlan's unaged ferrihydrites, whereas the fresher samples are notably more metastable.

Table 4.2 Thermodynamic cycle for high temperature oxide melt solution calorimetry for ferrihydrites

	Reactions – $FeOOH{\cdot}nH_2O$ formation enthalpy from elements and from oxides	**Enthalpy, ΔH (kJ/mol)**
1	$FeOOH{\cdot}nH_2O_{(s,25°C)} = \frac{1}{2}\alpha - Fe_2O_{3_{(sln,700°C)}} + \left(\frac{1}{2}+n\right)H_2O_{(g,700°C)}$	$\Delta H_1 = \Delta H_{ds1}$*
2	$\alpha - Fe_2O_{3_{(s,25°C)}} = \alpha - Fe_2O_{3_{(sln,700°C)}}$	$\Delta H_2 = 95.63 \pm 0.50$ [4]
3	$H_2O_{(l,25°C)} = H_2O_{(g,700°C)}$	$\Delta H_3 = 69.0$ [5]
4	$2Fe_{(s,25°C)} + \frac{3}{2}O_{2_{(g,25°C)}} = \alpha - Fe_2O_{3_{(s,25°C)}}$	$\Delta H_4 = -826.2 \pm 1.3$ [5]
5	$H_{2_{(g,25°C)}} + \frac{1}{2}O_{2_{(g,25°C)}} = H_2O_{(l,25°C)}$	$\Delta H_5 = -285.8 \pm 0.1$ [5]
6	$Fe_{(s,25°C)} + \left(1+\frac{n}{2}\right)O_{2_{(g,25°C)}} + \left(\frac{1}{2}+n\right)H_{2_{(g,25°C)}} = \alpha - FeOOH{\cdot}nH_2O_{(s,25°C)}$	$\Delta H_6 = \Delta H^o_{f,el}$ (FeOOH·nH2O)
7	$\frac{1}{2}\alpha - Fe_2O_{3_{(s,25°C)}} + \left(\frac{1}{2}+n\right)H_2O_{(l,25°C)} = FeOOH{\cdot}nH_2O_{(s,25°C)}$	$\Delta H_7 = \Delta H^o_{f,ox}$ (FeOOH·nH2O)
	$\boldsymbol{\Delta H_{f,el}, FeOOH{\cdot}nH_2O = \Delta H_6 = -\Delta H_1 + \frac{1}{2}\Delta H_2 + \left(\frac{1}{2}+n\right)\Delta H_3 + \frac{1}{2}\Delta H_4 + \left(\frac{1}{2}+n\right)\Delta H_5}$ $\boldsymbol{\Delta H_{f,ox}, FeOOH{\cdot}nH_2O = \Delta H_7 = -\Delta H_1 + \frac{1}{2}\Delta H_2 + \left(\frac{1}{2}+n\right)\Delta H_3}$	

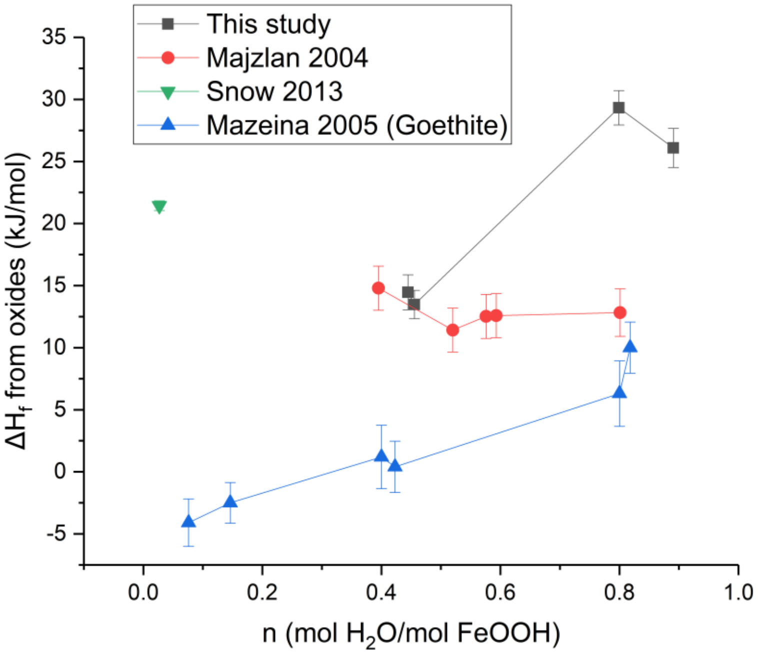

Figure 4.9 Formation enthalpies relative to binary oxides (α-Fe_2O_3 and H_2O) of ferrihydrites and goethite as a function of excess water content.

Formation enthalpies of ferrihydrites and goethite from multiple studies are compared as a function of excess water content (**Figure 4.3**). Enthalpies of formation from oxides for Majzlan's samples were within error of each other, i.e. there does not appear to be a dependence with respect to excess water content. This could be attributed to the particles being relatively "fresh" and structurally similar to each other. Ferrihydrites from Majzlan precipitated during constant titration up to a period of 24 hours, as opposed to gradual crystallization and coarsening for up to two years. As a result, these samples likely lose water content from forced aggregation of particles that lacked any notable opportunity to crystallize.

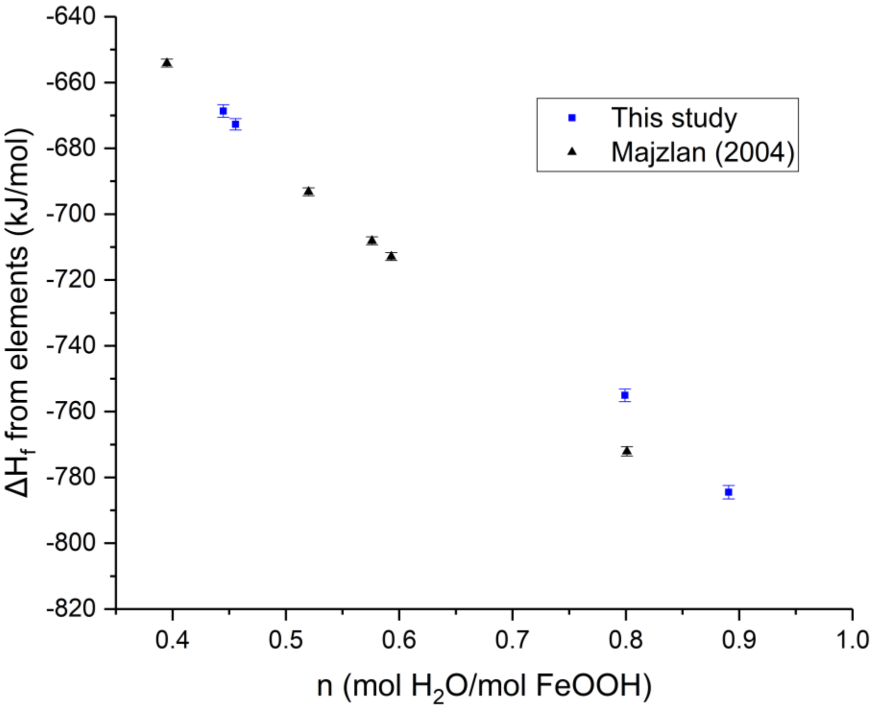

Figure 4.10 Formation enthalpies of ferrihydrites from elements as a function of excess water content.

Enthalpies of formation from oxides of goethite data (Mazeina et al. 2005) are compared as a function of water content. Those results demonstrate a similar slope to that of the present ferrihydrites, albeit all values are unsurprisingly shifted ltoward less endothermic values , reflecting the greater stability of goethite than ferihydrite. Particle sizes are reported in these results, and water content unsurprisingly scale with corresponding surface areas. Such data have not yet been collected for the present ferrihydrites.

Heats of formation from elements are linearly dependant on extent of hydration of the samples (**Figure 4.4**). The decrease in hydration with increasing aging time may be a result of gradual coarsening and reduction of surface sites of the ferrihydrite nanoparticles. The overwhelming dependence on water content is revealed by comparing formation enthalpies of Majzlan's samples – which are in good agreement with ferrihydrites from the current study. Majzlan et al. noted that the slope (-289.2 kJ/mol·nH_2O) corresponds to formation enthalpy of liquid water (-285.8 kJ/mol), which indicates weak interactions between the water and ferrihydrite surfaces.[6] Similarly, the current ferrihydrites fit along a slope of -279.4 kJ/mol·nH_2O. For reference, a nearly anhydrous ferrihydrite (n = 0.027 mol H_2O) by Snow et al. also falls along the trendline despite the extreme deviation from typical hydration values.[2] Such results are unsurprising and only validate that water content overshadows finer differences between each ferrihydrite sample.

4.4 Conclusions and Next Steps

At this point, calorimetric results indicate that aging has a notable effect on the stability of ferrihydrites. However, it is not yet clear what mechanisms contribute to this behavior. The difference of stabilities between our and Majzlan's ferrihydrite samples, despite similar range of water content, highlights the need for further characterization. Some hypothesized contributions include differences in crystallinity, morphology, and surface energetics. Contrubitions from surface area and corresponding surface energies are likely to be significant. Detailed structural and spectroscopic characterization of the same samples used for calorimetry is highly desirable.

If still available, it may be worth characterizing the ferrihydrites used in Majzlan's study to see how they may have changed after 16 years. Detailed spectroscopy, microscopy, and crystallography on these legacy samples may also provide useful information.

4.5 References

1. Majzlan, J., Navrotsky, A. & Schwertmann, U. Thermodynamics of iron oxides: Part III. Enthalpies of formation and stability of ferrihydrite (~$Fe(OH)_3$), schwertmannite (~$FeO(OH)_{3/4}(SO_4)_{1/8}$), and ε-$Fe_2O_3$. *Geochim. Cosmochim. Acta* **68**, 1049–1059 (2004).
2. Snow, C. L. *et al.* Heat capacity and thermodynamics of a synthetic two-line ferrihydrite, FeOOH·0.027H2O. *J. Chem. Thermodyn.* **58**, 307–314 (2013).
3. Mazeina, L. & Navrotsky, A. Surface enthalpy of goethite. *Clays Clay Miner.* **53**, 113–122 (2005).
4. Majzlan, J., Navrotsky, A. & Neil, J. M. Energetics of anhydrite, barite, celestine, and anglesite: A high-temperature and differential scanning calorimetry study. *Geochim. Cosmochim. Acta* **66**, 1839–1850 (2002).
5. Richard A. Robie & Hemingway, B. S. Thermodynamic Properties of Minerals and Related Substances at 298.15 K and 1 bar (105 pascals) and at Higher Temperatures. *U.S. Geol. Surv.* (1995).
6. Chase, M. W. NIST-JANAF Thermochemical Tables, 4th Ed. J. Phys. Chem. Ref. Data. 1998, Monograph 9 (Part I and Part II). *Journal of Physical and Chemical Reference Data* **Monograph**, Part I&II (1998).

Chapter 5

Conclusions and Future Directions

5.1 Conclusions

The structures and stabilities of two uranium-substituted iron (oxyhydr)oxide nanoscale polymorphs were characterized: α-Fe_2O_3 and α-FeOOH. To accomplish this, synthesis methods were developed for phase-pure samples with tunable concentrations of immobilized uranium. The thermodynamic stability of their precursor, ferrihydrite, was also studied as a function of aging time in solution.

Hydrothermal treatment was found to be an effective means of producing high quality uranium-substituted ferric oxides. Both polymorphs contained elevated concentrations of uranium that are recalcitrant to remobilization under acidic aqueous environments. This may serve as a potential means of water remediation and uranium leachate storage using benign, environmentally abundant minerals. The local coordination of uranium within the crystal structure of each polymorph was found to have some distinctions from previous studies that emulated conditions in radioactive waste environments. However, like in other studies, uranium was still found to occupy iron sites within each structure. These findings demonstrated that the local coordination of immobilized uranium is dependent on the conditions that led to its incorporation and coprecipitation with the host oxides.

Thermodynamic results indicated that uranium substitution into naturally ubiquitous rust products is possible, albeit with considerable energy penalties. It is possible that these values and trends may not translate well to samples with differences in local structure from uranium incorporation – such as those produced under emulated radiological waste disposal environments. Formation enthalpies relative to binary oxides reveal these products to be consistently stable relative to constituent elements, but metastable relative to binary oxides (**Figure 5.1**). Increasing uranium concentration consistently resulted in more positive formation enthalpies, with goethite demonstrating the most positive (least favorable) formation enthalpies at any given uranium concentration.

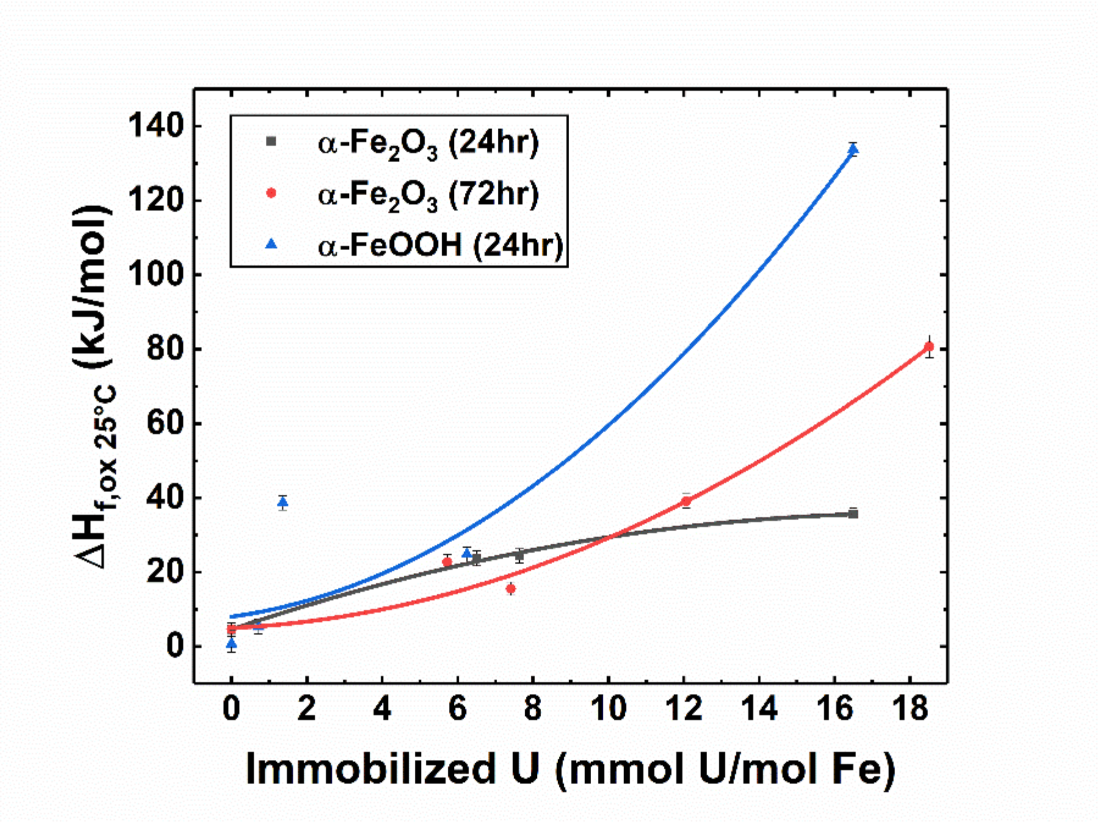

Figure 5.1 Formation enthalpies of uranium-incorporated hematite (α-Fe_2O_3) and goethite (α-FeOOH) calculated relative to binary oxides.

5.2 Future Directions

This research is worth further exploring for two primary reasons. The first is to understand the role of iron oxides, either by deliberate placement as an absorbent barrier or by natural oxidation of steel waste containers, in inhibiting the spread of toxic radioactive leachate. Understanding the thermodynamics of this mechanism is critical for assessing the feasibility of these materials in retaining radionuclides over the timescales necessary for them to decay into less harmful species.

As evidenced by the work on hematite, extended times at elevated temperatures resulted in higher relative amounts of well-immobilized uranium. It is apparent that hydrothermal treatment of hematite and goethite in the presence of uranyl ions had not reached equilibrium at elevated temperatures. Additional work on both hematite and goethite systems is needed to explore equilibrium points during hydrothermal treatment. Based on results from the hematite study, extended hydrothermal treatment times may allow for greater concentrations of uranium incorporation and greater corresponding enthalpic penalties. Meanwhile, goethite work did not explore the time dependence of uranium incorporation and its effect on underlying structure and thermodynamics. However, the overall enthalpic trend as a function of uranium content appears to follow that of hematite treated for 72 hours. Extended hydrothermal treatment times, beyond the studied 24 hours per batch, may elucidate a saturation point. In doing so, equilibrium may be reached, and the corresponding entropic contribution may be studied.

The groundwork has been laid for further studying iron oxide polymorphs in the presence of uranium. The varying oxidation states and complexes observable in radioactive waste environments can have critical consequences for uranium retention pathways, host mineral structure, and overall stability of immobilized solids. Early work has been performed on magnetite (Fe_3O_4) and anaerobic goethite (α-FeOOH), although with limited success and inconclusive results. Determining the thermodynamics of uranium-incorporated magnetite is highly desirable, as it may form under naturally occurring environments, and its magnetic properties are advantageous for aqueous uranium immobilization and extraction from water. Meanwhile, thermodynamic studies of Fe(II)-induced U-incorporated goethite could highlight different immobilization mechanisms and resulting local coordination of the uranium. Achieving high purity goethite samples with U(IV) and/or U(V) species within its structure may result in appreciably different thermodynamic stabilities compared to those presented in this work. Combining structural and thermodynamic data from present and future studies may provide a comprehensive, quantitative understanding of aqueous actinide immobilization across iron oxide stability landscapes.

Modifying experimental conditions to better represent environmental conditions with competing species should also be explored in the future. Uranyl complexation under varying aqueous environments (e.g., pH, carbonate and phosphate complexations, and competing cation species) may affect initial interactions with ferrihydrite colloids and resulting retention capacity through iron oxide crystallization. Structural and thermodynamic studies on the formation of mixed cation species within iron oxides should then be explored. It may be worth exploring whether the presence of another incorporated species can enhance or worsen uranium accommodation within each the structure of each polymorph, and whether the mixing of incorporated species may affect the overall stability of the host oxides.

Appendix A

Supporting Information for Chapter 2: Synthesis and Thermodynamics of Uranium-Incorporated α-Fe_2O_3 Nanoparticles

Figure SI-1 TEM imaging revealing faceted α-Fe_2O_3 nanoparticles.

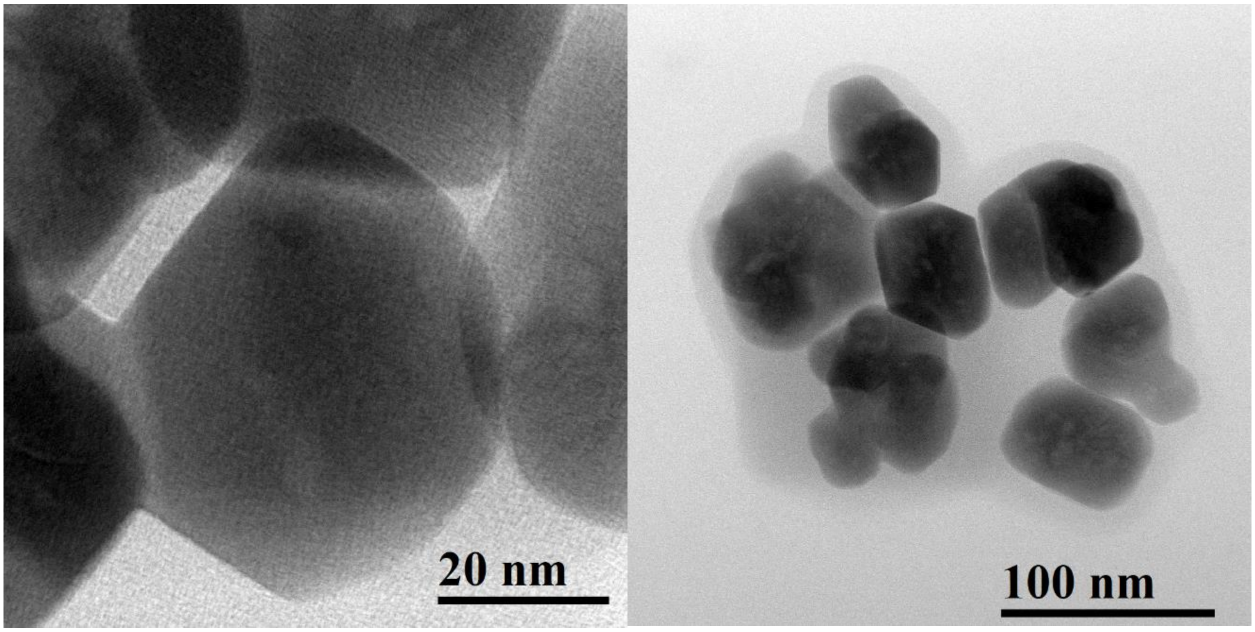

Figure SI-2 TEM imaging of crystallinity (left) and Z-contrast from U(VI) occupation along lattice fringes (right).

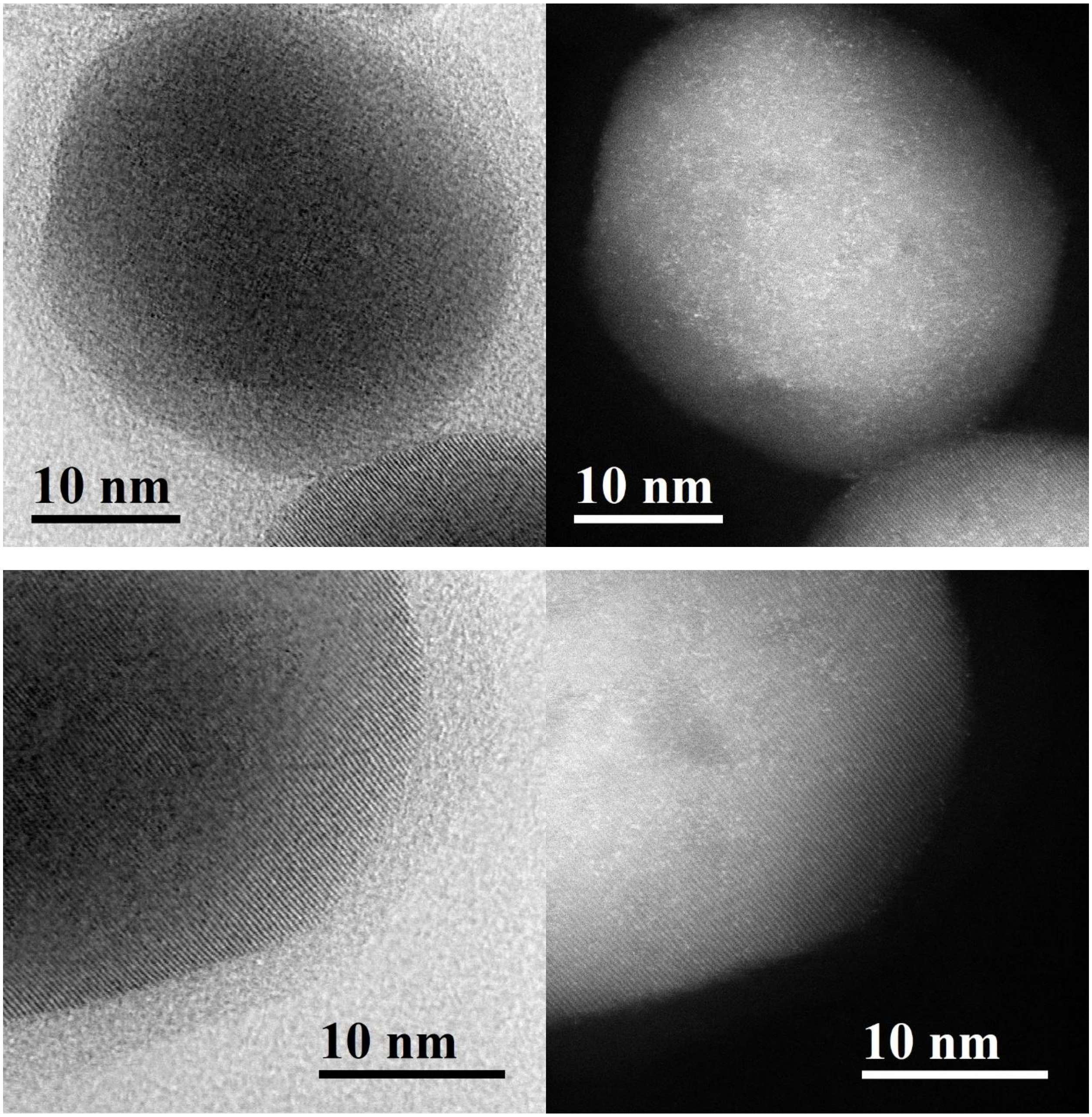

Figure SI-3 EDX mapping of constituent elements in U-incorporated α-Fe_2O_3.

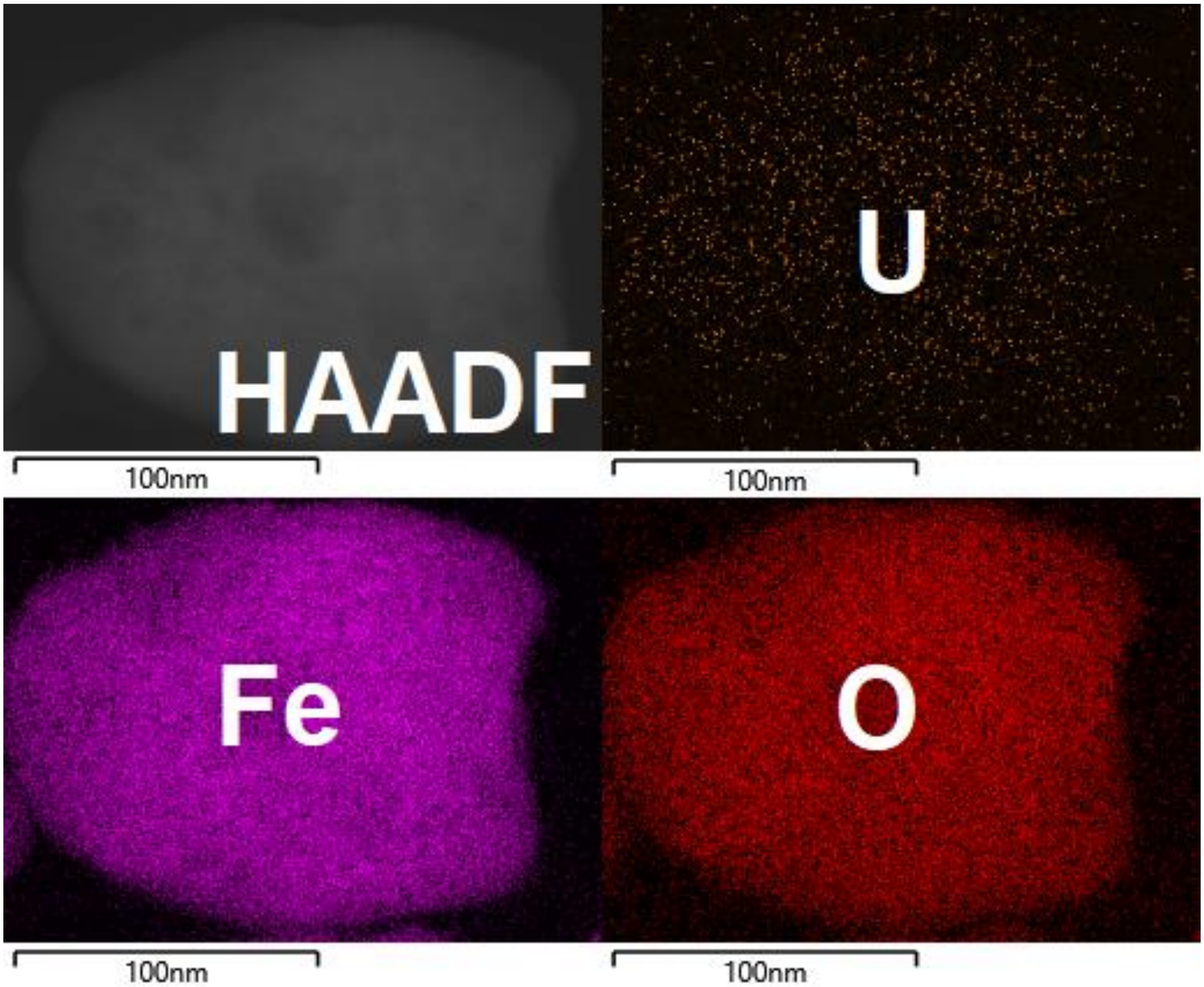

Figure SI-4 Concurrent TGA and DSC traces representative of $U_xFe_{2-2x}O_3$ synthesized using 24-hour and 72-hour hydrothermal treatment times.

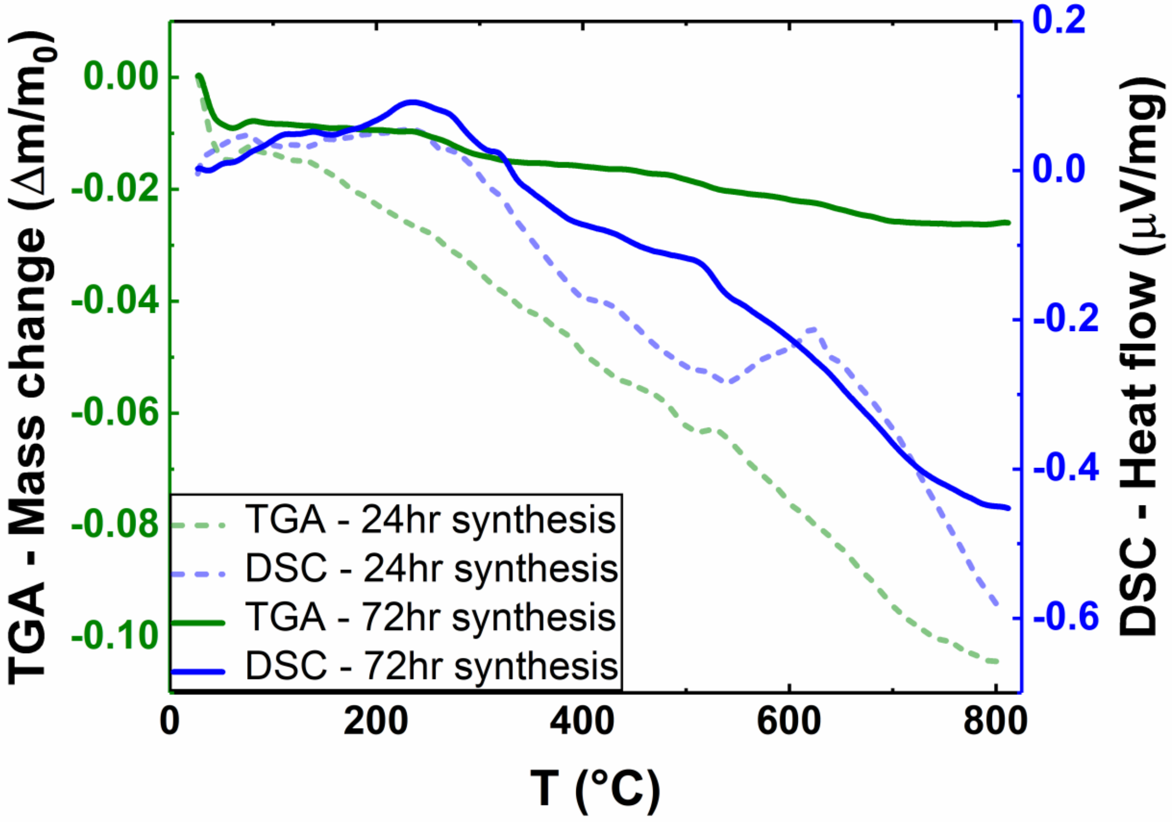

Table SI-1 F-test fit parameters

(a) Best fit

Path	CN	R (Å)	σ^2 (Å^2)	ΔE_0 (eV)	S0^2	χ_v^2	R
O_{Axial}	1.9	**1.79(4)**	0.006(4)	-3.0 ± 1.9	1	130.5	0.0195
$O_{Equitorial-1}$	2.2	**2.07(6)**	0.010(1)				
$O_{Equitorial-2}$	1.9	**2.21(4)**	0.010(1)				
Fe_{Edge}	2.8	**3.09(1)**	0.006(9)				
$Fe_{Corner-1}$	2.0	**3.27(4)**	0.007(2)				
$Fe_{Corner-2}$	2.0	**3.50(4)**	0.010(7)				
Fe_{Cell2}	1.0	**4.11(5)**	0.010(7)				

(b) Removing Fe_{Edge}

Path	CN	R (Å)	σ^2 (Å^2)	ΔE_0 (eV)	S0^2	χ_v^2	R
O_{Axial}	1.9	**1.78(9)**	0.006(3)	-4.6 ± 3.2	1	280.2	0.0417
$O_{Equitorial-1}$	2.2	**2.06(9)**	0.009(8)				
$O_{Equitorial-2}$	1.9	**2.20(5)**	0.009(8)				
~~Fe_{Edge}~~							
$Fe_{Corner-1}$	2.0	**3.07(8)**	0.005(8)				
$Fe_{Corner-2}$	2.0	**3.25(8)**	0.008(8)				
Fe_{Cell2}	1.0	**3.49(7)**	0.008(8)				

(c) Removing $\mathrm{Fe}_{\mathrm{Corner-1}}$

Path	CN	R (Å)	σ^2 (Å^2)	ΔE_0 (eV)	$S0^2$	χ_v^2	R
$\mathrm{O}_{\mathrm{Axial}}$	1.9	**1.77(9)**	0.006(0)	-5.4 ± 3.3	1	294.6	0.0497
$\mathrm{O}_{\mathrm{Equitorial-1}}$	2.2	**2.06(1)**	0.009(0)				
$\mathrm{O}_{\mathrm{Equitorial-2}}$	1.9	**2.20(6)**	0.009(0)				
$\mathrm{Fe}_{\mathrm{Edge}}$	2.8	**3.08(6)**	0.009(9)				
~~$\mathrm{Fe}_{\mathrm{Corner-1}}$~~							
$\mathrm{Fe}_{\mathrm{Corner-2}}$	2.0	**3.32(1)**	0.028(6)				
$\mathrm{Fe}_{\mathrm{Cell2}}$	1.0	**4.06(8)**	0.011(4)				

(d) Removing $\mathrm{Fe}_{\mathrm{Corner-2}}$

Path	CN	R (Å)	σ^2 (Å^2)	ΔE_0 (eV)	$S0^2$	χ_v^2	R
$\mathrm{O}_{\mathrm{Axial}}$	1.9	**1.78(9)**	0.006(3)	-4.3 ± 3.1	1	277.6	0.0536
$\mathrm{O}_{\mathrm{Equitorial-1}}$	2.2	**2.07(0)**	0.010(0)				
$\mathrm{O}_{\mathrm{Equitorial-2}}$	1.9	**2.20(7)**	0.010(0)				
$\mathrm{Fe}_{\mathrm{Edge}}$	2.8	**3.08(3)**	0.008(1)				
$\mathrm{Fe}_{\mathrm{Corner-1}}$	2.0	**3.28(6)**	0.010(5)				
~~$\mathrm{Fe}_{\mathrm{Corner-2}}$~~							
$\mathrm{Fe}_{\mathrm{Cell2}}$	1.0	**3.51(7)**	0.010(5)				

(e) Removing Fe_{Cell2}

Path	CN	R (Å)	σ^2 (Å^2)	ΔE_0 (eV)	$S0^2$	χ_v^2	R
O_{Axial}	1.9	**1.79(3)**	0.006(3)	-3.4 ± 2.4	1	204.4	0.0283
$O_{Equitorial-1}$	2.2	**2.07(2)**	0.009(6)				
$O_{Equitorial-2}$	1.9	**2.21(3)**	0.009(6)				
Fe_{Edge}	2.8	**3.09(0)**	0.007(1)				
$Fe_{Corner-1}$	2.0	**3.27(9)**	0.007(5)				
$Fe_{Corner-2}$	2.0	**3.50(7)**	0.009(8)				
~~Fe_{Cell2}~~							

(f) *Adding* Fe_{Face}

Path	CN	R (Å)	σ^2 (Å^2)	ΔE_0 (eV)	$S0^2$	χ_v^2	R
O_{Axial}	1.9	**1.83(7)**	0.006(8)	8.6 ± 2.4	1	293.7	0.0357
$O_{Equitorial-1}$	2.2	**2.11(4)**	0.005(7)				
$O_{Equitorial-2}$	1.9	**2.28(9)**	0.005(7)				
Fe_{Edge}	2.8	**2.79(1)**	0.014(2)				
$Fe_{Corner-1}$	2.0	**3.18(5)**	0.014(7)				
$Fe_{Corner-2}$	2.0	**3.72(1)**	0.020(3)				
Fe_{Cell2}	1.0	**4.32(3)**	0.020(3)				
Fe_{Face}	1.0	**4.58(4)**	0.011(2)				

Table SI-2 F-test results. α represents confidence level of the specified fit being statistically distinct from the reference fit.

F Test	α (%)	Comment
(a) Best fit	N/A	Reference point for subsequent F-Test fits
(b) Removing Fe_{Edge}	99.6	Removing shell significantly worsens fit
(c) Removing $Fe_{Corner\text{-}1}$	99.7	Removing shell significantly worsens fit
(d) Removing $Fe_{Corner\text{-}2}$	100.0	Removing shell significantly worsens fit
(e) Removing Fe_{Cell2}	97.5	Removing shell significantly worsens fit
(f) Adding Fe_{Face}	98.7	Removing shell significantly improves fit

Appendix B

Supporting Information for Chapter 3: Aerobic synthesis and thermodynamics of uranium-incorporated α-FeOOH nanoparticles

Table SI-1 F-test fit parameters

(a) Best fit

Path	CN	R (Å)	σ^2 (Å^2)	ΔE_0 (eV)	$S0^2$	χ_v^2	R
$\mathrm{O_{Axial}}$	1.3	**1.81(9)**	0.004(3)	8.7 ± 1.0	1.0	3.141	0.010
$\mathrm{O_H}$	2.0	**2.22(5)**	0.004(0)				
$\mathrm{O_{Equitorial}}$	2.7	**2.41(4)**	0.004(0)				
$\mathrm{Fe_{Edge1}}$	1.8	**3.25(8)**	0.004(5)				
$\mathrm{Fe_{Edge2}}$	2.0	**3.45(9)**	0.004(5)				
$\mathrm{Fe_{Corner}}$	2.0	**3.65(4)**	0.005(8)				
$\mathrm{Fe_{C\text{-}C}}$	4	**5.32(8)**	0.006(5)				
$\mathrm{Fe_{E\text{-}C\text{-}C}}$	8	**5.56(9)**	0.011(5)				

(b) Removing $\mathrm{Fe_{Edge\text{-}1}}$

Path	CN	R (Å)	σ^2 (Å^2)	ΔE_0 (eV)	$S0^2$	χ_v^2	R
$\mathrm{O_{Axial}}$	1.3	**1.81(6)**	0.004(2)	8.4 ± 1.5	1.0	5.540	0.025
$\mathrm{O_H}$	2.0	**2.22(5)**	0.004(7)				
$\mathrm{O_{Equitorial}}$	2.7	**2.41(1)**	0.004(7)				
~~$\mathrm{Fe_{Edge\text{-}1}}$~~							
$\mathrm{Fe_{Edge\text{-}2}}$	2.0	**3.59(2)**	0.013(1)				
$\mathrm{Fe_{Corner}}$	3.0	**3.32(0)**	0.016(1)				
$\mathrm{Fe_{C\text{-}C}}$	4	**5.33(0)**	0.007(0)				
$\mathrm{Fe_{E\text{-}C\text{-}C}}$	8	**6.54(8)**	0.011(7)				

(c) Removing $\text{Fe}_{\text{Edge-2}}$

Path	CN	R (Å)	σ^2 (Å^2)	ΔE_0 (eV)	$S0^2$	χ_v^2	R
O_{Axial}	1.3	**1.81(7)**	0.004(2)	8.6 ± 1.5	1.0	5.197	0.023
O_{H}	2.0	**2.22(6)**	0.004(7)				
$\text{O}_{\text{Equitorial}}$	2.7	**2.41(3)**	0.004(7)				
$\text{Fe}_{\text{Edge-1}}$	1.8	**3.28(8)**	0.011(5)				
~~$\text{Fe}_{\text{Edge-2}}$~~							
$\text{Fe}_{\text{Corner}}$	3.0	**3.58(0)**	0.015(8)				
$\text{Fe}_{\text{C-C}}$	4	**5.33(1)**	0.006(9)				
$\text{Fe}_{\text{E-C-C}}$	8	**5.57(3)**	0.011(7)				

(d) Removing $\text{Fe}_{\text{Corner}}$

Path	CN	R (Å)	σ^2 (Å^2)	ΔE_0 (eV)	$S0^2$	χ_v^2	R
O_{Axial}	1.3	**1.81(7)**	0.004(2)	8.6 ± 1.5	1.0	5.276	0.023
O_{H}	2.0	**2.22(6)**	0.004(7)				
$\text{O}_{\text{Equitorial}}$	2.7	**2.41(3)**	0.004(7)				
$\text{Fe}_{\text{Edge-1}}$	1.8	**3.28(7)**	0.011(3)				
$\text{Fe}_{\text{Edge-2}}$	2.2	**3.57(6)**	0.015(8)				
~~$\text{Fe}_{\text{Corner}}$~~							
$\text{Fe}_{\text{C-C}}$	4	**5.33(1)**	0.006(9)				
$\text{Fe}_{\text{E-C-C}}$	8	**5.57(3)**	0.011(7)				

(e) Removing remote Fe (corner-corner)

Path	CN	R (Å)	σ^2 (Å^2)	ΔE_0 (eV)	$S0^2$	χ_v^2	R
O_{Axial}	1.3	**1.81(9)**	0.004(3)	8.7 ± 1.3	1.0	4.473	0.026
O_H	2.0	**2.22(5)**	0.004(1)				
$O_{Equitorial}$	2.7	**2.41(4)**	0.004(1)				
Fe_{Edge-1}	1.8	**3.25(6)**	0.004(7)				
Fe_{Edge-2}	2.2	**3.45(8)**	0.004(8)				
Fe_{Corner}	3.0	**3.65(2)**	0.006(0)				
~~Fe_{C-C}~~							
Fe_{E-C-C}	8	**5.82(3)**	0.047(1)				

(f) Removing remote Fe (edge-corner-corner)

Path	CN	R (Å)	σ^2 (Å^2)	ΔE_0 (eV)	$S0^2$	χ_v^2	R
O_{Axial}	1.3	**1.81(9)**	0.004(3)	8.8 ± 1.3	1.0	4.467	0.023
O_H	2.0	**2.22(6)**	0.004(2)				
$O_{Equitorial}$	2.7	**2.41(4)**	0.004(2)				
Fe_{Edge-1}	1.8	**3.25(7)**	0.004(7)				
Fe_{Edge-2}	2.2	**3.45(8)**	0.004(8)				
Fe_{Corner}	3.0	**3.65(3)**	0.006(0)				
Fe_{C-C}	4	**5.29(4)**	0.013(3)				
~~Fe_{E-C-C}~~							

Table SI-2 F-test results. α represents confidence level of the specified fit being statistically distinct from the reference fit.

F Test	α (%)	Comment
(a) Best fit	N/A	Reference point for subsequent F-Test fits
(b) Removing Fe_{Edge1}	100.0	Removing shell significantly worsens fit
(c) Removing Fe_{Edge2}	100.0	Removing shell significantly worsens fit
(d) Removing Fe_{Corner}	100.0	Removing shell significantly worsens fit
(e) Removing Fe_{CC}	100.0	Removing shell significantly worsens fit
(f) Removing F_{ECC}	100.0	Removing shell significantly worsens fit

Table SI-3 Thermochemical reactions for calculating formation enthalpies of α-$U_{0.5x}Fe_{1-x}OOH$.

	Reactions - Enthalpy of formation of $U_{0.5x}Fe_{1-x}OOH$ from elements and from oxides at 25°C	Enthalpy, ΔH (kJ/mol)	Ref.
1	$U_{0.5x}Fe_{1-x}OOH_{(s,25^\circ C)} \rightarrow \frac{x}{2}UO_{3_{(sln,700^\circ C)}} + \frac{(1-x)}{2}Fe_2O_{3(sln,700^\circ C)} + \frac{1}{2}H_2O_{(g,700^\circ C)}$ for $0 < x < 0.016$	$\Delta H_1 = \Delta H_{ds}$	
2G	$\alpha - FeOOH_{(s,25^\circ C)} \rightarrow \frac{1}{2}Fe_2O_{3(sln,700^\circ C)} + \frac{1}{2}H_2O_{(g,700^\circ C)}$	$\Delta H_{2G} = 84.68 \pm 0.9$	1,2
2H	$\alpha - Fe_2O_{3(s,25^\circ C)} \rightarrow Fe_2O_{3(sln,700^\circ C)}$	$\Delta H_{2H} = 95.63 \pm 0.50$	1
3	$H_2O_{(l,25^\circ C)} \rightarrow H_2O_{(g,700^\circ C)}$	$\Delta H_3 = 69.0$	1
4	$O_{2(g,25^\circ C)} \rightarrow O_{2(g,700^\circ C)}$	$\Delta H_4 = 21.83$	1
5a	$\gamma - UO_{3(s,25^\circ C)} \rightarrow UO_{3(sln,700^\circ C)}$	$\Delta H_{5a} = 9.49 \pm 1.53$	3
5b	$\frac{1}{3}U_3O_{8(s,25^\circ C)} + \frac{1}{6}O_{2(g,25^\circ C)} \rightarrow UO_{3(sln,700^\circ C)}$	$\Delta H_{5b} = 54.0 \pm 6.4$	3
5c	$UO_{2(s,25^\circ C)} + \frac{1}{2}O_{2(g,25^\circ C)} \rightarrow UO_{3(sln,700^\circ C)}$	$\Delta H_{5c} = -140.4 \pm 0.67$	3
6	$2Fe_{(s,25^\circ C)} + \frac{3}{2}O_{2(g,25^\circ C)} \rightarrow \alpha - Fe_2O_{3(s,25^\circ C)}$	$\Delta H_6 = -826.2 \pm 1.3$	4
7	$U_{(s,25^\circ C)} + \frac{3}{2}O_{2(g,25^\circ C)} \rightarrow \gamma - UO_{3(s,25^\circ C)}$	$\Delta H_7 = -1223.8 \pm 0.8$	4
8	$H_{2(g,25^\circ C)} + \frac{1}{2}O_{2(g,25^\circ C)} \rightarrow H_2O_{(l,25^\circ C)}$	$\Delta H_8 = -285.8 \pm 0.1$	4
9a	$(1-x)(\alpha - FeOOH)_{(s,25^\circ C)} + \boldsymbol{\frac{x}{2}UO_{3_{(s,25^\circ C)}}} \rightarrow U_{0.5x}Fe_{1-x}OOH_{(s,25^\circ C)}$	$\Delta H_{9a} = \Delta H_{f,ox-G1}$	
9b	$(1-x)(\alpha - FeOOH)_{(s,25^\circ C)} + \boldsymbol{\frac{x}{6}U_3O_{8(s,25^\circ C)}} \rightarrow U_{0.5x}Fe_{1-x}OOH_{(s,25^\circ C)}$	$\Delta H_{9b} = \Delta H_{f,ox-G2}$	
9c	$(1-x)(\alpha - FeOOH)_{(s,25^\circ C)} + \boldsymbol{\frac{x}{2}UO_{2_{(s,25^\circ C)}}} \rightarrow U_{0.5x}Fe_{1-x}OOH_{(s,25^\circ C)}$	$\Delta H_{9c} = \Delta H_{f,ox-G3}$	
10a	$\frac{(1-x)}{2}\alpha - Fe_2O_{3(s,25^\circ C)} + \boldsymbol{\frac{x}{2}UO_{3_{(s,25^\circ C)}}} + \frac{1}{2}H_2O_{(l,25^\circ C)} \rightarrow U_{0.5x}Fe_{1-x}OOH_{(s,25^\circ C)}$	$\Delta H_{10a} = \Delta H_{f,ox-H1}$	
10b	$\frac{(1-x)}{2}\alpha - Fe_2O_{3(s,25^\circ C)} + \boldsymbol{\frac{x}{6}U_3O_{8(s,25^\circ C)}} + \frac{1}{2}H_2O_{(l,25^\circ C)} \rightarrow U_{0.5x}Fe_{1-x}OOH_{(s,25^\circ C)}$	$\Delta H_{10b} = \Delta H_{f,ox-H2}$	
10c	$\frac{(1-x)}{2}\alpha - Fe_2O_{3(s,25^\circ C)} + \boldsymbol{\frac{x}{2}UO_{2_{(s,25^\circ C)}}} + \frac{1}{2}H_2O_{(l,25^\circ C)} \rightarrow U_{0.5x}Fe_{1-x}OOH_{(s,25^\circ C)}$	$\Delta H_{10c} = \Delta H_{f,ox-H3}$	
11	$\frac{x}{2}U_{(s,25^\circ C)} + (1-x)Fe_{(s,25^\circ C)} + \frac{1}{2}H_2O_{(l,25^\circ C)} + \frac{3}{4}O_{2(g,25^\circ C)} \rightarrow U_{0.5x}Fe_{1-x}OOH_{(s,25^\circ C)}$	$\Delta H_{11} = \Delta H_{f,el}$	
	$\Delta H_{f,ox-G1} = -\Delta H_1 + (1-x)\,\Delta H_{2G} + \frac{x}{2}\,\Delta H_{5a}$ $\Delta H_{f,ox-G2} = -\Delta H_1 + (1-x)\,\Delta H_{2G} + \frac{x}{2}\,\Delta H_{5b}$ $\Delta H_{f,ox-G3} = -\Delta H_1 + (1-x)\,\Delta H_{2G} + \frac{x}{2}\,\Delta H_{5c}$ $\Delta H_{f,ox-H1} = -\Delta H_1 + \frac{(1-x)}{2}\,\Delta H_{2H} + \frac{1}{2}\,\Delta H_3 + \frac{x}{2}\,\Delta H_{5a}$ $\Delta H_{f,ox-H2} = -\Delta H_1 + \frac{(1-x)}{2}\,\Delta H_{2H} + \frac{1}{2}\,\Delta H_3 + \frac{x}{2}\,\Delta H_{5b}$ $\Delta H_{f,ox-H3} = -\Delta H_1 + \frac{(1-x)}{2}\,\Delta H_{2H} + \frac{1}{2}\,\Delta H_3 + \frac{x}{2}\,\Delta H_{5c}$ $\Delta H_{f,el} = -\Delta H_1 + \frac{1}{2}\,[(1-x)\,\Delta H_{2H} + \Delta H_3 + \frac{3}{2}\,\Delta H_4 + x\,\Delta H_{5a} + (1-x)\,\Delta H_6 + x\,\Delta H_7 + x\,\Delta H_8]$ **for $\boldsymbol{0 < x < 0.016}$ mol U**		

Figure SI-1 Standard formation enthalpies of $U_{0.5x}Fe_{1-x}OOH$ in relation to α-Fe_2O_3 and binary uranium oxides of varying oxidation states.

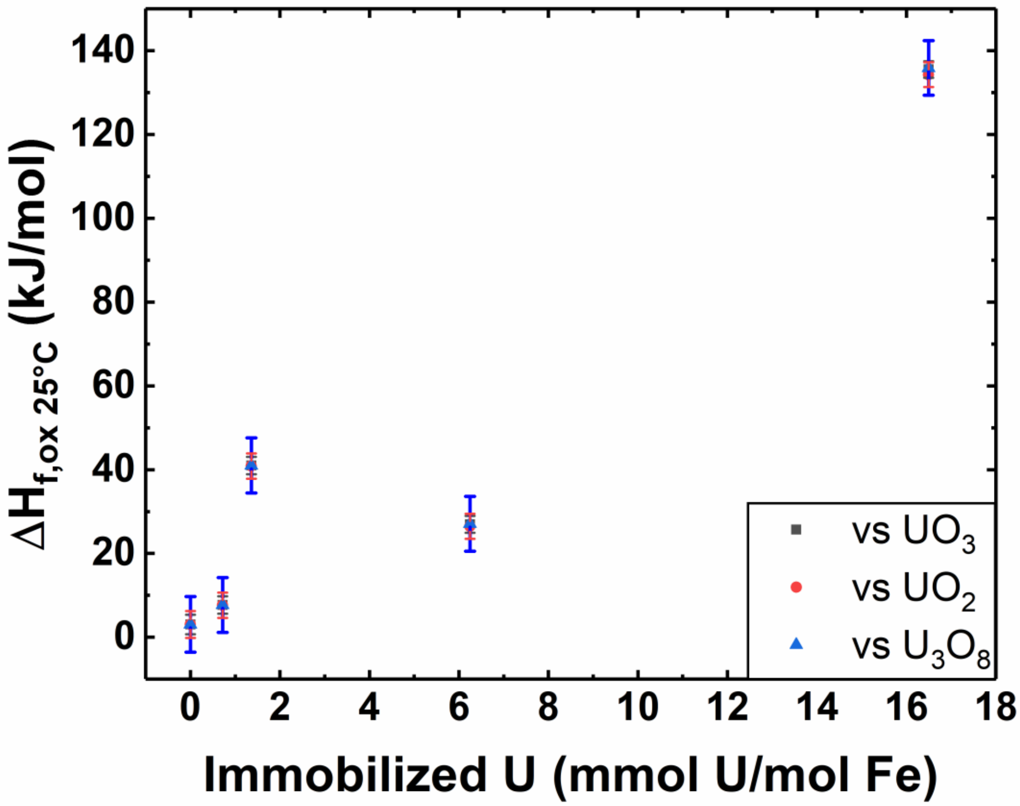

References

1. Chase, M. W. NIST-JANAF Thermochemical Tables, 4th Ed. J. Phys. Chem. Ref. Data. 1998, Monograph 9(Part I and Part II). *Journal of Physical and Chemical Reference Data* **Monograph**, Part I&II (1998).

2. Mazeina, L. & Navrotsky, A. Surface enthalpy of goethite. *Clays Clay Miner.* **53**, 113–122 (2005).

3. Guo, X. *et al.* Thermodynamics of formation of coffinite, USiO 4. *Proc. Natl. Acad. Sci.* **112**, 6551–6555 (2015).

4. Richard A. Robie & Hemingway, B. S. Thermodynamic Properties of Minerals and Related Substances at 298.15 K and 1 bar (105 pascals) and at Higher Temperatures. *U.S. Geol. Surv.* (1995).